

# The Na-O anticorrelation in horizontal branch stars. IV. M 22 <sup>★,★★</sup>

R.G. Gratton<sup>1</sup>, S. Lucatello<sup>1</sup>, A. Sollima<sup>2</sup>, E. Carretta<sup>2</sup>, A. Bragaglia<sup>2</sup>, Y. Momany<sup>1,3</sup>, V. D’Orazi<sup>4,5</sup>, S. Cassisi<sup>6,7</sup>, and M. Salaris<sup>8</sup>

<sup>1</sup> INAF-Osservatorio Astronomico di Padova, Vicolo dell’Osservatorio 5, I-35122 Padova, Italy

<sup>2</sup> INAF-Osservatorio Astronomico di Bologna, Via Ranzani 1, I-40127, Bologna, Italy

<sup>3</sup> European Southern Observatory, Alonso de Cordova 3107, Vitacura, Santiago, Chile

<sup>4</sup> Department of Physics & Astronomy, Macquarie University, Balaclava Rd., North Ryde, Sydney, NSW 2109, Australia

<sup>5</sup> Monash Centre for Astrophysics, School of Mathematical Sciences, Building 28, Monash University, VIC 3800, Australia

<sup>6</sup> INAF-Osservatorio Astronomico di Teramo, Via Collurania, Teramo, Italy

<sup>7</sup> Instituto de Astrofísica de Canarias, La Laguna, Tenerife, Spain

<sup>8</sup> Astrophysics Research Institute, Liverpool John Moores University, Twelve Quays House, Birkenhead, UK

## ABSTRACT

We obtained high-resolution spectra for 94 candidate stars belonging to the HB of M 22 with FLAMES. Previous works have indicated that this cluster has split subgiant (SGB) and red giant branches (RGB) and hosts two different stellar populations, differing in overall metal abundance and both exhibiting a Na-O anti-correlation. The HB stars we observed span a restricted temperature range ( $7,800 < T_{\text{eff}} < 11,000$  K), where about 60% of the HB stars of M 22 are. Within our sample, we can distinguish three groups of stars segregated (though contiguous) in colours: Group 1 (49 stars) is metal-poor, N-normal, Na-poor and O-rich: our abundances for this (cooler) group match very well those determined for the primordial group of RGB stars (a third of the total) from previous studies. Group 2 (23 stars) is still metal-poor, but it is N- and Na-rich, though only very mildly depleted in O. We can identify this intermediate group as the progeny of the metal-poor RGB stars that occupy an intermediate location along the Na-O anti-correlation and include about 10% of the RGB stars. The third group (20 stars) is metal-rich, Na-rich, and O-rich. This hotter group likely corresponds to the most O-rich component of the previously found metal-rich RGB population (a quarter of the total). We did not observe any severely O-depleted stars and we think that the progeny of these stars falls on the hotter part of the HB. Furthermore, we found that the metal-rich population is also over-abundant in Sr, in agreement with results for corresponding RGB and SGB stars. However, we do not find any significant variation in the ratio between the sum of N and O abundances to Fe. We do not have C abundances for our stars. There is some evidence of an enhancement of He content for Groups 2 and 3 stars ( $Y = 0.338 \pm 0.014 \pm 0.05$ ); the error bar due to systematics is large, but a consistent analysis of data for several GCs confirms that stars in these groups within M 22 are likely overabundant in He. We conclude that on the whole, our results agree with the proposition that chemical composition drives the location of stars along the HB of a GC. Furthermore, we found a number of fast rotators. They are concentrated in a restricted temperature range along the HB of M 22. Fast rotating stars might be slightly less massive and bluer than slowly rotating ones, but other interpretations are possible.

**Key words.** Stars: abundances – Stars: evolution – Stars: Population II – Galaxy: globular clusters – Galaxy: individual: M22

## 1. Introduction

Low-mass core He-burning stars show a wide distribution in the colour-magnitude diagram of globular clusters (GCs) along the so-called horizontal branch (HB). This distribution primarily reflects variations in masses and the chemical composition of stars, with a minor but not negligible part being played by the stars’ evolution off their initial location on the zero age horizontal branch (ZAHB). Full understanding of the reasons individual stars occupy a given position along the ZAHB has still not been achieved, probably because several different mechanisms are involved simultaneously. This constitutes the “second parameter problem” (Sandage & Wildey 1967; van den Bergh 1967), and the first parameter is metallicity, which is responsible for most of the observational variance (Sandage & Wallerstein 1960; Faulkner 1966). Important progress has been made thanks

to the understanding that significant star-to-star variations can be expected in the helium content within individual GCs, which are made of different stellar populations (see Ventura et al. 2001; Bedin et al. 2004; D’Antona et al. 2005; Norris 2004; Piotto et al. 2005, following much earlier suggestions by e.g. Rood 1973 and Norris et al. 1981). Older and/or He-richer stars are expected to leave the main sequence phase with lower masses. If they lose a similar amount of mass as younger and/or He-normal stars along the RGB, they are expected to be less massive, that is, bluer, when on the HB. There is a broad correlation between extension of the HB and properties very likely related to He abundances, such as the extension of the Na-O anti-correlation (Na-rich and O-poor stars are expected to be more He-rich than Na-poor and O-rich ones; Carretta et al. 2007), both driven mainly by the total mass of the GCs (Recio-Blanco et al. 2006).

A few years ago, we (Gratton et al. 2010; see also Dotter 2013 for a review of this and later contributions) presented a quite extensive re-analysis of the distribution of stars along the HB of several tens GCs and found that a combination of variations in age (from cluster-to-cluster) and He-content (from star-to-star within a cluster), added to metallicity, may indeed explain most of the variance in the HB morphology. This was achieved

Send offprint requests to: R.G. Gratton, raffaele.gratton@oapd.inaf.it

\* Based on observations collected at ESO telescopes under programmes 087.D-0230 and 091.D-0151

\*\* Tables 3, 4, 5, and 6 are only available in electronic form at the CDS via anonymous ftp to cdsarc.u-strasbg.fr (130.79.128.5) or via [http://cdsweb.u-strasbg.fr/cgi-bin/qcat?J/A+A/???/???/???](http://cdsweb.u-strasbg.fr/cgi-bin/qcat?J/A+A/???/???)

by adopting a simple universal relation between the total mass lost along the RGB and metallicity, with a small (but not negligible) star-to-star random contribution (one-two hundredths of solar masses, about 10% of the total mass lost along the RGB). The presence of this last random term most likely implies that even if the scenario considered by Gratton et al. were broadly correct, something still needs to be added in order to achieve very accurate predictions. Potential candidates, whose importance has not yet been well established, include variations in the CNO/Fe abundance ratio, core rotation, and binarity. The list of potential parameters is even longer, see Fusi Pecci & Bellazzini (1997) and Catelan (2009) for more comprehensive summaries.

A corollary of the star-to-star He abundance variations explanation for the distribution of stars along the HB of an individual GC is that there should be correlations between temperatures and chemical abundances, only partly fuzzed by evolution off the ZAHB. Such correlations can be retrieved through spectroscopy of HB stars. However, spectra of HB stars are difficult to analyse. Ever since the pioneering work of Peterson (1983) we know that rotation can be present on the BHB. Furthermore, abundances for stars hotter than about 11,000 K (the so-called Grundahl-jump, Grundahl et al. 1999) are heavily affected by diffusion and radiative levitation (e.g. Behr et al. 1999, Mohler 2001; Moni Bidin et al. 2006).

Villanova et al. (2009) first tried to connect spectroscopic determinations of the composition of stars along the HB of NGC 6752 with the multiple population scenarios and were also able to obtain information about He, though with non-negligible error bars, finding a low He abundance consistent with the cosmological value, as expected for the kind of stars observed. In fact, He-rich stars are expected to be hotter than the Grundahl-jump in most old and metal-poor GCs in order to avoid too bright HB's at the RR Lyrae colours, as has been known for several decades (see e.g. Iben 1968; Cassisi et al. 2003; Salaris et al. 2004; and the review by Catelan 2009). Two other papers on M 4 (Marino et al. 2011a; Villanova et al. 2012) have confirmed what has been found by Villanova et al. (2009): red HB stars (RHB: that is, stars redder than the RR Lyrae instability strip) are Na-poor and O-rich, while BHB stars are Na-rich and O-poor. Furthermore, the observed BHB stars of M 4, which are amongst the warmest in that cluster, are more He-rich than the stars observed in NGC 6752.

In this series of papers we present the analysis of wide samples of HB stars for a few important GCs. Table 1 gives a summary of main results obtained in published papers. In Gratton et al. (2011) we considered NGC 2808; as in M 4, which has similar metallicity, RHB stars are O-rich, but they show a spread in Na abundances correlated with temperature. Blue HB stars cooler than the Grundahl-jump are (moderately) O-poor and Na-rich. These results have been confirmed by Marino et al. (2013b) using higher S/N spectra, from which they also derived He abundances and finding quite a high value of  $Y \sim 0.34 \pm 0.01 \pm 0.05$  for BHB stars. Even He-richer stars should be present, but they should be hotter than the Grundahl-jump (D'Antona et al. 2005), so this cannot be verified directly. Gratton et al. (2012a) studied NGC 1851, which is a complex GC with a split SGB (Milone et al. 2009), two populations slightly differing in their Fe-content (Carretta et al. 2010, 2011), and related to the bright (b-)SGB (metal-poor) and the faint (f-)SGB (metal-rich: Gratton et al. 2012b), and two distinct Na-O anti-correlations (Carretta et al. 2010, 2011). Also the bimodal HB of NGC 1851 is complex, with the RHB stars separated into two groups. The vast majority are O-rich and Na-poor, while about 10-15% are Na-rich and moderately O-poor. A separate Na-O anti-correlation is seen

among BHB stars. We suggested that most BHB stars descend from the f-SGB stars and are older and that most RHB stars descend from the b-SGB ones and are younger, but the correspondence is probably not one-to-one. Finally, 47 Tuc and M 5 were discussed in Gratton et al. (2013). The cluster 47 Tuc is a simpler case, with a clear correlation between the location on the HB and the Na and O abundances (i.e. like M 4). Instead, while RHB stars in M 5 are invariably Na-poor and O-rich, the case is more complex for BHB stars, and the lack of a tight correlation between colours and chemical composition for these stars requires some additional mechanism to explain observations.

In this paper we focus on M 22 (=NGC 6656), a very intriguing GC. Marino et al. (2009, 2011) show that there are two populations in this cluster with different values of  $[\text{Fe}/\text{H}]$ , robustly confirming findings based on calcium (Da Costa et al. 2009; Lee et al. 2009). The two populations can be identified with the two SGBs (Marino et al. 2009, 2012): the metal-poor RGB population is the descendant of the b-SGB, and the metal-rich one of the f-SGB. Both populations display a separate Na-O anti-correlation. The metal-rich population also appears to be much richer in  $s$ -process elements, and Marino et al. (2012) suggest that it is also richer in the sum of the CNO elements, a fact that could help explain the split SGB since at a given age and metallicity, stars richer in CNO elements are fainter on the SGB. These properties of M 22 closely resemble those of NGC 1851, but its predominantly blue HB does not present the striking bi-modality seen in the latter, maybe because of the different metal content ( $[\text{Fe}/\text{H}] = -1.70$  for M 22 vs  $[\text{Fe}/\text{H}] = -1.18$  for NGC 1851: Harris, 1996). Two recent papers have studied the HB of M 22: a high dispersion study of seven among the coolest non-variable HB stars of M 22 has been presented by Marino et al. (2013a), while Salgado et al. (2013) employed low-resolution blue spectra to measure masses over a large portion of the HB. Marino et al. (2013a) found that all these stars are Ba-poor and Na-poor. This favours the hypothesis that the position of a star along the HB is strictly related to the chemical composition and that these stars all belong to the first (Na-poor and He-normal) portion of the metal-poor population of M 22. This agrees with an analysis of the whole colour-magnitude diagram by Joo & Lee (2013), who identified BHB stars with the metal-poor population and the extreme BHB stars with the metal-rich one. According to these last authors, a large difference in helium abundance ( $Y = 0.23$  to  $0.32$ ) is required to explain the HB. Our analysis allows extending the study of Marino et al. (2013a) to a much larger sample of HB stars.

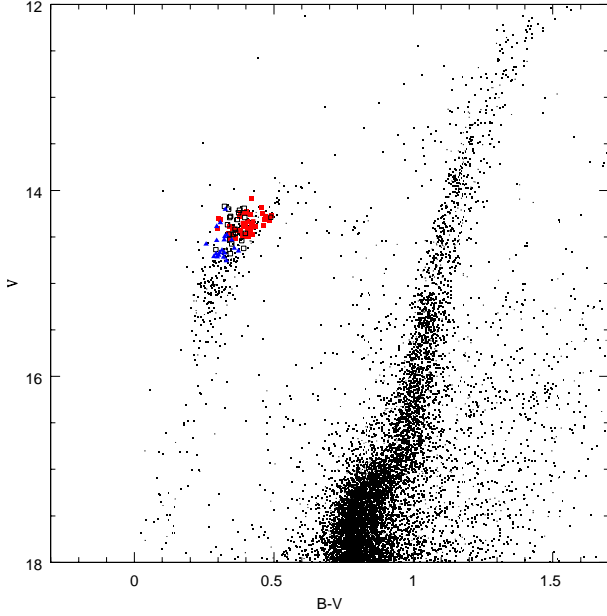
Section 2 presents the observations and data reduction, explaining how they differ from what has been done for the other GCs studied in this series. Derivation of the atmospheric parameters and detail of the abundance analysis are given in Section 3. Section 4 presents the results and assignment of the stars to three different populations based on a statistical cluster analysis. Section 5 presents a discussion of the HB of this cluster based on these results and on a comparison with evolutionary models. Conclusions are drawn in Section 6.

## 2. Observations

The present analysis is based on spectra obtained with the GIRAFFE spectrograph of the FLAMES multi-object facility at the VLT UT2 Kueyen telescope (Pasquini et al. 2004). FLAMES was used in MEDUSA mode, with individual fibres pointed to

**Table 1.** Summary of results on Na-O abundances along the HB in various clusters

Cluster	Red HB	Blue HB
47 Tuc (Gratton et al. 2013)	[Na/O] correlates with colour (increases as B-V decreases)	
NGC 1851 (Gratton et al. 2012a)	Mostly O-rich/Na-poor 10-15% Na-rich, moderately O-poor Mostly descendants from b-SGB	Na-rich/O-poor (Na-O anticorrelation) Mostly descendants from f-SGB
NGC 2808 (Gratton et al. 2011)	O-rich Spread Na (correlated with colour)	Moderately O-poor Moderately Na-rich
M 5 (Gratton et al. 2013)	Na-poor, O-rich	Na-O anticorrelation Most stars with abundances similar to RHB stars

**Fig. 1.**  $(V, B - V)$  colour-magnitude diagram of M 22 from Monaco et al. (2004). Different symbols are for stars of different groups (see Section 4): Group 1: red filled squares; Group 2: black open squares; Group 3: blue filled triangles. Dots are the stars not observed in this paper.**Table 2.** Observing log

Set up HR	Date	UT Start	Exp. time (s)	Airmass	Seeing (arcsec)
3	2013-04-25	05:27:57	2400	1.53	1.14
3	2013-04-25	06:09:42	2400	1.30	1.25
3	2013-07-06	07:49:52	2400	1.47	2.19
3	2013-07-10	02:56:02	2400	1.04	0.92
3	2013-08-01	03:12:40	2400	1.01	0.91
3	2013-08-01	04:37:01	2400	1.12	0.77
12	2011-09-11	03:16:50	1500	1.41	1.29
19A	2011-06-29	07:21:31	2500	1.21	1.84

stars or empty sky positions. Spectra were obtained with three different set ups: HR03 (wavelength range 4033-4201 Å, resolution  $R \sim 24,800$ ), HR12 (wavelength range 5821-6146 Å, resolution  $R \sim 18,700$ ), and HR19A (wavelength range 7745-8335 Å, resolution  $R \sim 13,867$ ). The HR12 and HR19A set ups were selected to allow observations of the strongest features of Na I (the D resonance doublet) and O I (the 7771-74 Å high ex-

citation triplet) observable in metal-poor BHB stars, other lines of the same elements being too weak in such stars. High excitation lines of N I and Mg II are also present in these spectral regions. To unambiguously separate the two main populations of M 22 (the metal-poor one, related to the bright SGB, and the metal-rich one, to the faint SGB), we then asked for additional observing time with the HR03 set up, giving access to several strong Fe I features and the resonance line of Sr II at 4077 Å, which is the strongest feature of an element produced by  $n$ -capture processes. In addition, this spectral region provides data on Mg I, Si II, Ti II, Fe II, and H $\delta$ , which could be used to derive a reddening-free temperature index. This also allowed solving ambiguities related to differential reddening when analysing the spectra. The journal of observations is in Table 2.

We focussed our attention on the BHB between the blue edge of the instability strip (at an effective temperature of about 7800 K) and the Grundahl jump (at an effective temperature of 11,000 K), though our faint limit actually is slightly brighter than the Grundahl jump. Cooler stars, most of them RR Lyrae variables, were avoided because scheduling their observation at the appropriate phases required for the analysis would have been impractical. Hotter stars were also not included because their abundances are affected by the impact of microscopic diffusion and radiative levitation. When we considered the photometry by Monaco et al. (2004) over 424 bona fide HB stars, we counted 28 stars (that is 7%) with  $(B - V)_0 > 0.15$ , hence within the instability strip; 221 stars (52%) with  $(B - V)_0 < 0.15$  and with  $M_V < 14.8$ , that is, within the range of our spectroscopic sample; and 175 stars (41%) fainter stars. Counting stars on the  $vby$  photometry of the cluster from Richter et al. (1999), kindly provided by the authors, we found that in their photometry (which covers an area of M 22 similar to the one we are considering here) there are 71 stars (that is, 32% of total) bluer than the Grundahl jump, 138 stars (61% of total) in the observed range, and 16 redder stars (7% of total). The small difference between star counts of Monaco et al. and Richter et al. most likely depends on different definition of the photometric limits. These numbers (and their uncertainties) should be taken into account when interpreting our results in terms of the stellar populations of M 22 (see Section 5).

We were able to point fibres on 94 stars, selected from the photometry by Monaco et al. (2004). The location of these stars on the colour-magnitude diagram is shown in Figure 1. The stars were selected to have no neighbour within 2 arcsec that are brighter than  $M_{\text{target}} + 2.5$  mag than the target star. One of the stars (#130 on our notation) was revealed to be a field star from its discrepant radial velocity. It also has much stronger lines than the stars of M 22. An additional star (#114 on our notation), though clearly a cluster member, is a small amplitude (0.04 mag) variable (star KT-51 in the Kaluzny & Thompson 2001 list). When

analysed as the other programme stars are, it yielded odd results, very likely due to large temperature variations during our observations, which span a few years. All remaining observed stars yielded consistent radial velocity and are likely members of M 22, whose radial velocity of  $-146.3 \text{ km s}^{-1}$  (Harris et al. 1996) sets them far from expectations for most field stars. Fourteen fibres were pointed to empty sky locations.

We collected photometric data for the programme stars from various sources: broad band *BVI* photometry based on data acquired with the WFI camera at the ESO 2.2m telescope (Monaco et al. 2004); *vby* Strömgren photometry by Richter et al. (1999), kindly provided by the authors; and 2MASS *JHK* photometry (Skrutskie et al. 2006). These photometric data were dereddened using the reddening map by Monaco et al. (2004). Relevant data are listed in Table 3. While we do not list errors for individual stars for the *vby* photometry, paper, upper limits for the total photometric errors are 0.015 mag for *V*, 0.019 mag for  $(b - y)$ , and 0.029 mag for  $m_1$ , according to Richter et al. (1999).

Exposure times were set to provide  $S/N \sim 50$  for all the observed spectral ranges. Observations longer than 45 minutes were then split into several visits that were performed over several months. Spectra were extracted and calibrated using the ESO FLAMES/GIRAFFE pipeline v 2.11.1, running under GASGANO environment (available at <http://www.eso.org/sci/software/pipelines/>). Sky subtraction, combination, continuum normalization, and shifting to rest frame were performed with IRAF<sup>1</sup>. A median of the sky spectra was obtained. Different spectra for the same star were cross correlated with respect to the first exposure and brought to common radial velocity before being combined using the median over different exposures (the spectra have similar shapes and flux levels); we then applied the barycentric correction of the first spectrum. Shift to rest wavelength was done using the radial velocities measured in the spectra. A normalisation was done on the spectra using CONTINUUM task within IRAF with a third-order Legendre function.

### 2.1. Radial velocities

We measured radial velocities from the co-added spectra obtained with individual set ups (see Table 4). They were measured using Gaussian fitting to the position of three to eight lines in each spectrum and the same lines were used for all stars. Since very few spectral lines are detectable, radial velocities have quite large errors: comparison of different spectra yields typical errors of  $\pm 2.4 \text{ km s}^{-1}$  for set-up HR03 and HR19A (see Figure 2), while typical errors are twice as large for set-up HR12. Weighted averages have typical errors of  $\pm 1.7 \text{ km s}^{-1}$ , fully adequate both as a membership criterion and for comparison of the scatter we obtain within different groups of stars with the overall dispersion of the radial velocities for the cluster, which we measured at  $7.7 \pm 0.8 \text{ km s}^{-1}$  for the HB stars we considered. This value (which includes measurement errors, which are however small) is almost coincident with the value of  $7.8 \pm 0.3 \text{ km s}^{-1}$  listed by Harris (1996). Since spectra with the HR03 set up were obtained two years later than those with the other two set-ups, variations in the radial velocity might be used to detect binaries. For two

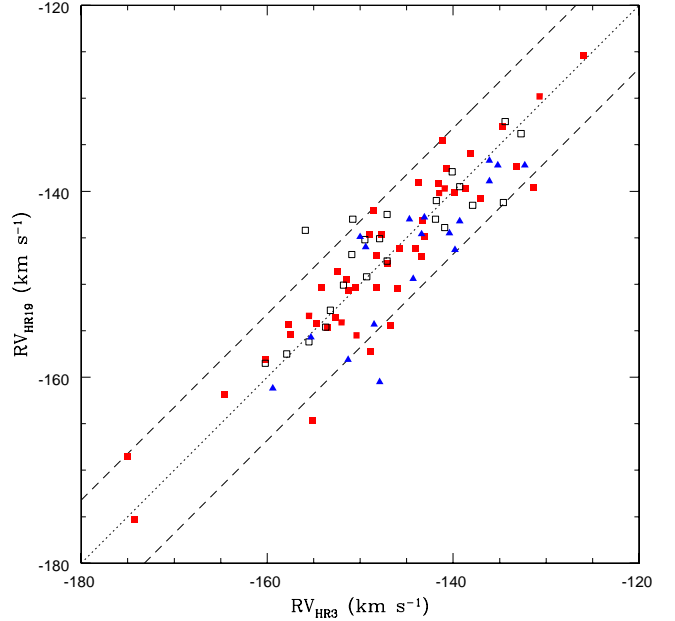


**Fig. 2.** Radial velocities from set-up HR03 vs those from set-up HR19A; different colours are for stars of different groups (see Section 4): Group 1: red filled squares; Group 2: black open squares; Group 3: blue filled triangles. Dotted line represents equality; dashed lines are  $\pm 2$  times the observational errors.

stars (#88 and #62), we obtained differences in radial velocities of  $-11.7$  and  $+12.6 \text{ km s}^{-1}$ , respectively, when comparing data obtained with HR03 and HD19A. These differences are about 3.5 times larger (in absolute value) than is typical for other stars: they are then candidate binaries. We notice, however, that both of them are quite fast rotators (see next section) and this makes their radial velocity measures more uncertain.

We may compare our radial velocities with those measured by Marino et al. (2013a) for the four stars in common between the two samples. On average, the difference (ours-Marino et al.) is  $0.3 \pm 1.6 \text{ km s}^{-1}$  (r.m.s.= $3.2 \text{ km s}^{-1}$ ). Most of the scatter is due to star #17 (for which we do not have the spectra with the HR03 set-up), which is star #166 in their notation. According to their discussion, this star is suspected of being a blue straggler star (BSS). BSS often show radial velocity variations, associated to binarity. If this star is dropped, on average the difference is  $-1.3 \pm 0.2 \text{ km s}^{-1}$ , with a very small r.m.s. scatter of only  $0.3 \text{ km s}^{-1}$ . We do not attribute much importance to the small zero point difference that is typical of observations with different set ups of GIRAFFE/UVES. The very small r.m.s. scatter supports our use of radial velocities for membership, internal dynamics, and binary detection. In addition, we have 14 stars in common with Salgado et al. (2013). While they do not claim high accuracy in their velocities, we found excellent agreement with ours, well within the errors they quoted. On average, our radial velocities are lower by  $11.1 \pm 1.7 \text{ km s}^{-1}$ , with an r.m.s. of  $6.3 \text{ km s}^{-1}$  for individual stars, which is much less than their quoted error of  $\pm 18 \text{ km s}^{-1}$ .

<sup>1</sup> IRAF is distributed by the National Optical Astronomy Observatories, which are operated by the Association of Universities for Research in Astronomy, Inc., under cooperative agreement with the National Science Foundation.

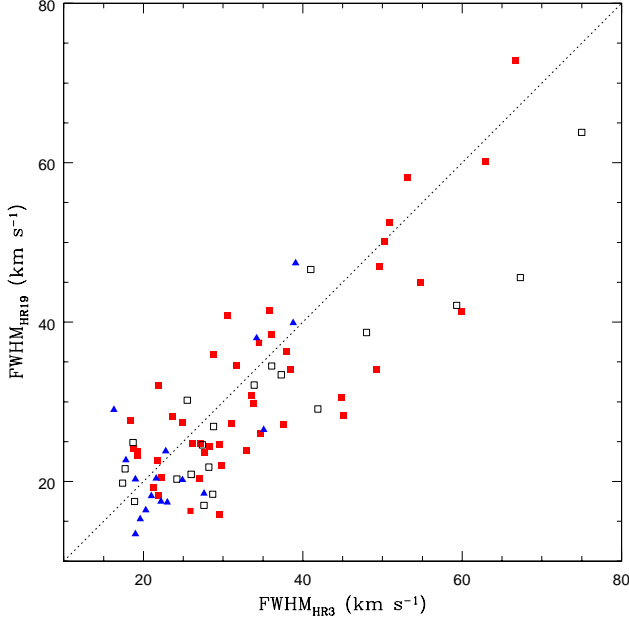


**Fig. 3.** FWHM of lines from set up HR03 vs those from set up HR19A; different colours are for stars of different groups (see Section 4): Group 1: red filled squares; Group 2: black open squares; Group 3: blue filled triangles.

## 2.2. Rotational velocities

We found that spectral lines of several stars are clearly broader than those of others. This is likely to be due to rotation (see Peterson 1983; Behr et al. 1999; Recio-Blanco et al. 2004). We then measured the full width at half maximum (FWHM) of the spectral lines, which is the convolution of the instrumental profile and intrinsic broadening of the spectral lines. The values we obtained from individual set ups are listed in Columns 10-12 of Table 4. The weighted average values (with double weight to results from set ups HR03 and HR19, where there are stronger lines) are given in Column 13, with their errors in Column 14. In Figure 3 we compare the FWHM of lines from set up HR03 to those from set up HR19A. There is quite a good correlation between these measures.

An accurate estimate of the errors in line broadening is complex, because it depends on line strength (hence temperature), S/N of the spectra, and spectral resolution, but this is beyond the scope of our work here. An order-of-magnitude estimate can be obtained by comparing results obtained with different set ups, after taking the different resolving power into account. Typical values are  $\pm 5 \text{ km s}^{-1}$ . The lower envelope of the distribution (with  $\text{FWHM} \sim 19 \text{ km s}^{-1}$ ) is likely to be populated by slowly rotating star, whose profile is dominated by instrumental broadening and turbulent motions. FWHM of the rotational broadening may then be obtained by deconvolution of the observed FWHM for this value. While our data are not calibrated for this purpose, we expect that for profiles dominated by rotational broadening  $v \sin i \sim \text{FWHM} / \sqrt{2}$ . We then derived values of  $v \sin i$  using the formula  $v \sin i = \sqrt{(\text{FWHM}^2 - \text{FWHM}_{\text{ins}}^2)/2}$ , where the second term takes the instrumental profile into account. The values of  $\text{FWHM}_{\text{ins}}$  we used were those appropriate for each set up. Wherever this formula yielded a value of  $v \sin i < 5 \text{ km s}^{-1}$ , we only gave an upper limit of  $5 \text{ km s}^{-1}$  to  $v \sin i$ . For the four stars

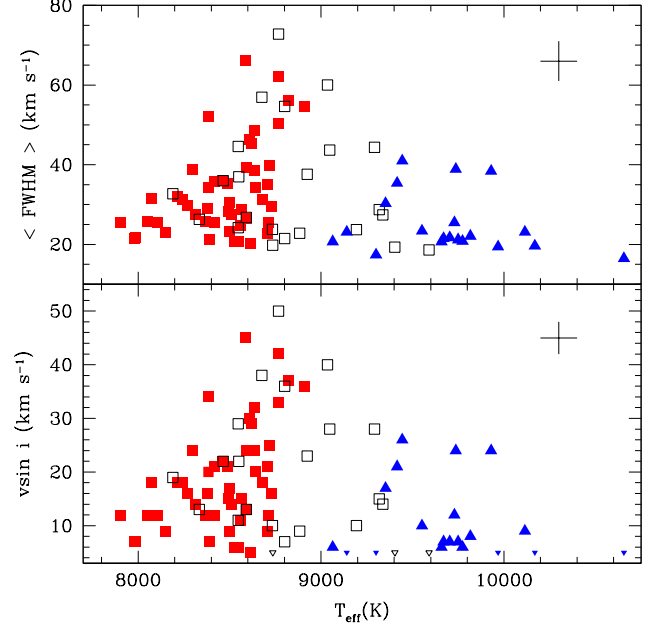


**Fig. 4.**  $T_{\text{eff}}$  vs FWHM of lines (upper panel) and rotational velocity ( $v \sin i$ : lower panel); different colours are for stars of different groups (see Section 4): Group 1: red filled squares; Group 2: black open squares; Group 3: blue filled triangles. Small triangles in the lower panel represent upper limits in  $v \sin i$ . Typical error bars are also shown.

in common with Marino et al. (2013a), we may compare values of  $v \sin i$  obtained with this rough procedure (listed in Column 15 of Table 4) with those they obtained from their higher resolution UVES spectra. On average, the difference (ours-Marino et al. 2013a) is  $\Delta v \sin i = -2 \pm 3 \text{ km s}^{-1}$  and the r.m.s. scatter of  $6 \text{ km s}^{-1}$  agrees quite well with our estimate of the errors.

The star with the broadest lines in our sample (#52) has a  $\text{FWHM} = 73 \text{ km s}^{-1}$ , which corresponds to a rotational velocity of  $v \sin i \sim 50 \text{ km s}^{-1}$ . This value is at the upper limit of the distribution for BHB stars (Peterson et al. 1995; Behr et al. 2000a, 2000b; Recio-Blanco et al. 2004; Lovisi et al. 2012).

Figure 4 shows the run of rotational velocities with effective temperatures. At any given temperature, there is some scatter in rotational velocities. The upper envelope of the distribution peaks at about 8800 K. The number of stars with evidence of rotation is a function of temperature: all fast rotators ( $\text{FWHM} > 40 \text{ km s}^{-1}$ ) are in the temperature range 8400-9400 K.

## 3. Analysis

### 3.1. Atmospheric parameters

Our analysis is based on model atmospheres extracted by interpolation within the Kurucz (1993) grid. Interpolations were done as described in Gratton & Sneden (1987) and used in many other



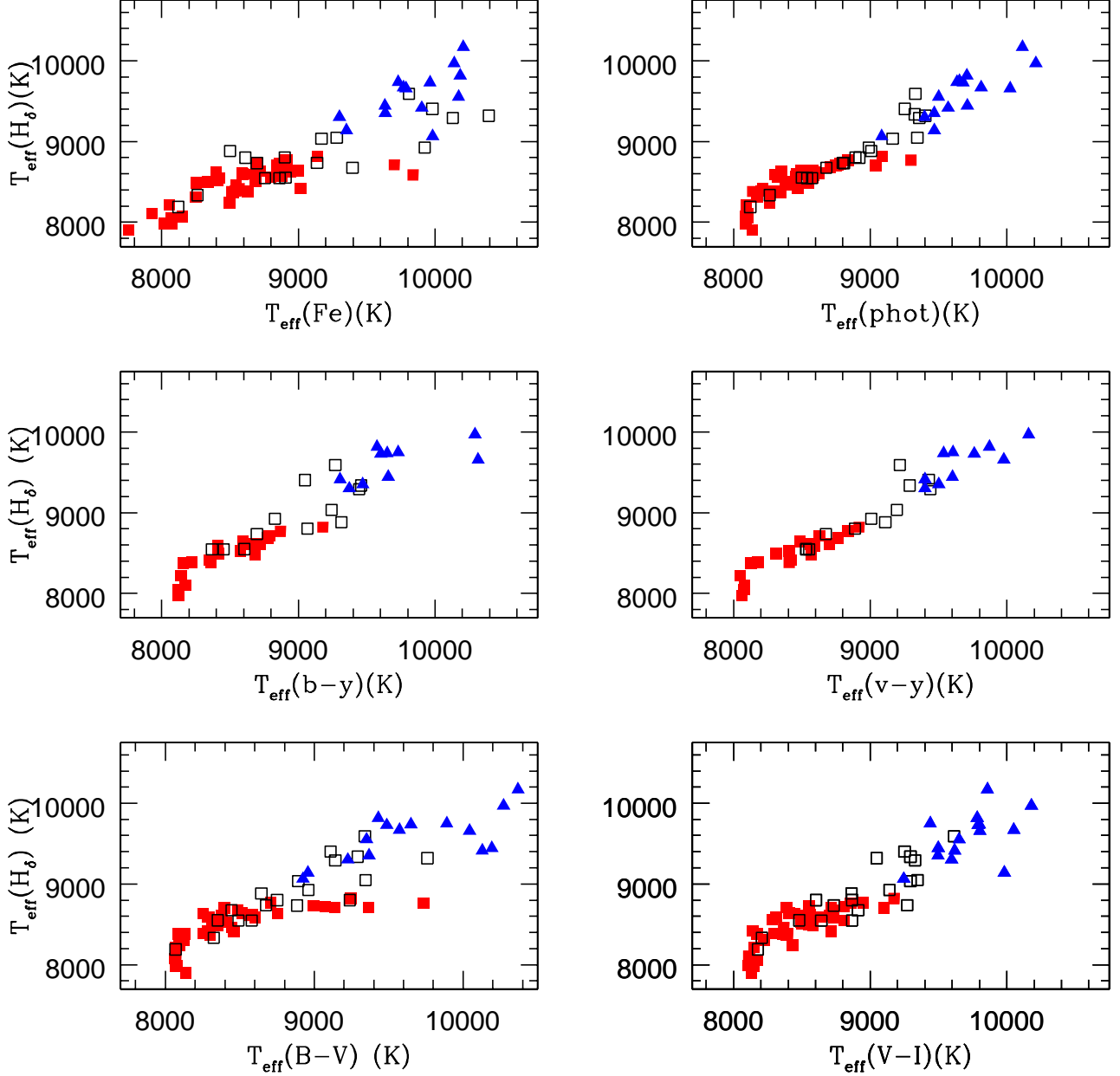


**Fig. 8.** Comparison between temperatures from colours and their average ( $T_{\text{eff}}(\text{phot})$ ) and from our calibration of the  $H\delta$  line ( $T_{\text{eff}}(H\delta)$ ). Different colours are for stars of different groups (see Section 4). Group 1: red filled squares; Group 2: black open squares; Group 3: blue filled triangles.

papers. The grid of models used for this interpolation does not include any alpha enhancement. However, at this high temperature, most of the electrons are provided by hydrogen, not metals. The impact of modifying model metal abundances is then very small, as confirmed by detailed calculations (see Section 3.5).

The most critical parameter in our abundance analysis is the effective temperature  $T_{\text{eff}}$ . In previous papers of this series (Gratton et al. 2011, 2012a, 2013),  $T_{\text{eff}}$ 's were derived from colours using calibrations that, for the BHB stars, were based on Kurucz (1993) model atmospheres. Since red-infrared colours saturate for such warm stars, most useful information is provided by visual and near-ultraviolet colours. Unfortunately, while BVI

data were available for all stars, violet colours were only available for about half of them, and we have no reliable UV photometry for a significant number of stars.

A basic problem in deriving colours for the programme stars is the variation in interstellar reddening over the field of M 22. M 22 is seen in projection against the Galactic bulge and has a high ( $E(B-V)=0.34$ ; Harris 1996) and differential reddening (e.g. Richter et al. 1999). A map of such variation has been prepared by Monaco et al. (2004) covering the whole field of interest. We then corrected our colours first for the average reddening of M 22 ( $E(B-V) = 0.34$ ; Harris, 1996) and then for the differential reddening provided by Monaco et al. (2004). We then

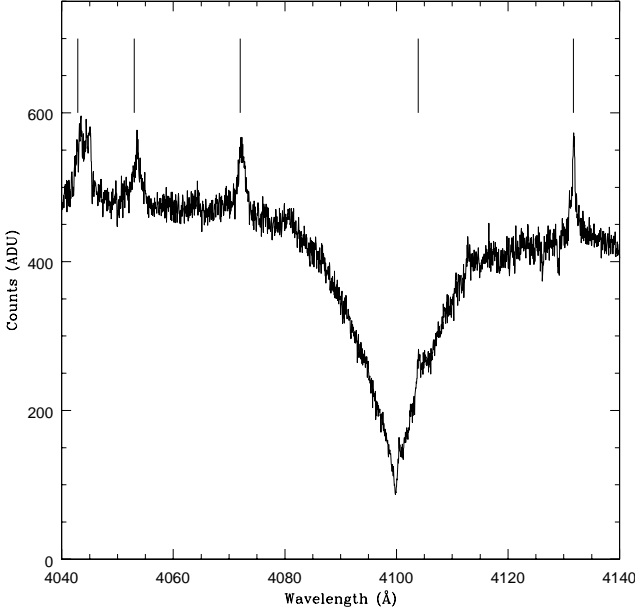


**Fig. 5.** Portion of the spectrum of star 115 including  $H_\delta$ . This is the most extreme case of stronger contamination by Th-Ar lines. Identification of several contaminating lines is from the Kitt Peak Th-Ar spectrum (<http://old-www.noao.edu/kpno/specatlas/thar/>)

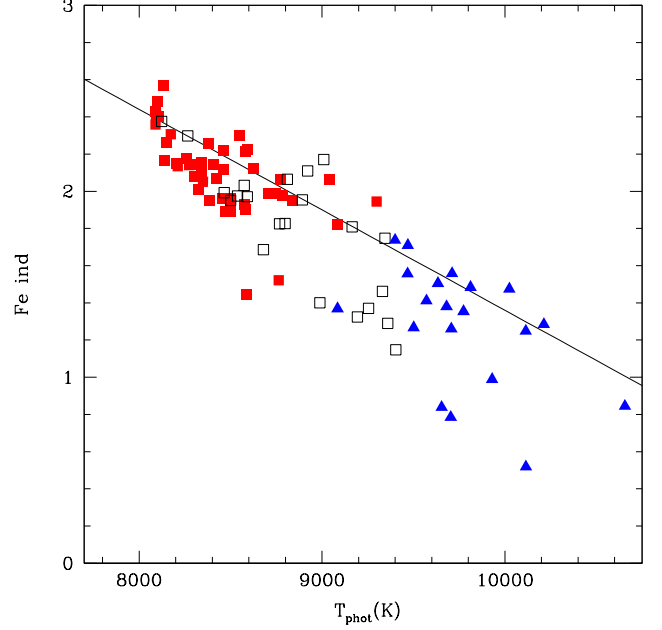


**Fig. 7.** Comparison between the Fe I line strength index Fe-Ind and temperatures from photometry ( $T_{\text{eff}}(\text{Phot})$ ). Different symbols are for stars of different groups (see Section 4): Group 1: red filled squares; Group 2: black open squares; Group 3: blue filled triangles. Superimposed is the calibration line we used.

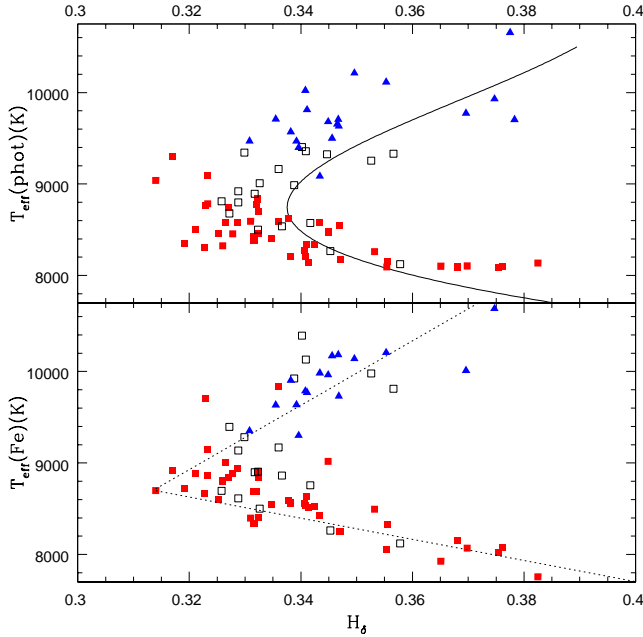


**Fig. 6.** Upper panel: Comparison between temperatures from photometry ( $T_{\text{eff}}(\text{Phot})$ ) and the index of the strength of the  $H_\delta$  line ( $H_\delta$ ); overimposed is the relation expected from theoretical models (see Munari et al. 2005). Lower panel: the same, but for temperatures from Fe lines ( $T_{\text{eff}}(\text{Fe})$ ). Different symbols are for stars of different groups (see Section 4): Group 1: red filled squares; Group 2: black open squares; Group 3: blue filled triangles. The fit lines used to define  $T_{\text{Cool}}$  and  $T_{\text{Hot}}$  are also plotted in the bottom panel.

derived temperatures from  $B - V$ ,  $V - I$ ,  $b - y$ , and  $v - y$  colours, reducing them to a consistent scale, which is the one defined by  $B - V$  colours. We also considered  $V - K$  colours, but later discarded them because errors were too large to be useful. We then made a weighted average of these temperatures, assigning double weight to  $v - y$  colours. We called  $T_{\text{eff}}(\text{phot})$  these estimates of the effective temperatures.

These photometric temperatures still contain non-negligible errors, owing not only to errors in the calibration and photometry of individual stars, but also to uncertainties in the differential reddening map, which are of the order of 0.01 mag in  $E(B - V)$ , which corresponds to several hundred K for BHB stars. Luckily, our spectra offer the opportunity to derive effective temperatures from the strength of  $H_\delta$ . Hydrogen lines in BHB stars are also sensitive to gravity (see e.g. discussion in Marino et al. 2013a); however, this effect does not cause a large scatter in the relation between effective temperature and strength of the line because the spread in mass and radius (and then surface gravity) at a given  $T_{\text{eff}}$  is actually very small. We then computed an index of the strength of  $H_\delta$  (which we called by this same name) that is the ratio of the flux within a region 8 Å wide centred on the line and of the average in two similar reference regions located symmetrically with respect to the line at 40 Å separation. We then plotted this  $H_\delta$  index against  $T_{\text{eff}}(\text{phot})$  (see Figure 6). For a few stars, contamination of the spectra by the wavelength calibration lamp falsifies this  $H_\delta$  index, while the spectra can still be used, with some care, for other purposes. This problem was found for nine stars. Figure 5 shows a portion of the spectrum of star 115 including  $H_\delta$ , which is the case of strongest contamination.

The parameter  $H_\delta$  shows a smooth run with  $T_{\text{eff}}(\text{phot})$ , with a minimum (i.e. strongest line) at about 8800 K. For comparison, we also plotted the observed relation with a calibration based on theoretical models in the upper panel of Figure 6; for this

purpose, we used the same definition of the indices to measure  $H_\delta$  indices on the theoretical spectral library by Munari et al. (2005). We interpolated the values of the indices we obtained for the observed run of gravity with temperature. On the whole, there is quite good agreement, though measured  $H_\delta$  index are slightly lower (that is, the line appears stronger) than given by the models. The difference is small and can be attributed to problems in how the continuum normalization was done on our spectra. We attribute the scatter around a mean relation to the effects of residual differential reddening. To support this claim, we constructed another spectroscopic index Fe-Ind that we designated as the logarithm of the sum of the equivalent widths of the three strongest Fe I lines observable in our spectra (at 4045.82, 4063.60, and 4071.75 Å), and also plotted this quantity against  $T_{\text{eff}}(\text{phot})$  (see Figure 7). We could then fit a straight line through the observed points and construct a temperature index that we called  $T_{\text{eff}}(\text{Fe})$ . Plotting  $H_\delta$  against  $T_{\text{eff}}(\text{Fe})$  (see Figure 6), we find that the scatter in the plot is considerably reduced. This is precisely what we expect if a significant source of scatter in the  $H_\delta - T_{\text{eff}}(\text{phot})$  plot is due to differential reddening that was not properly taken into account.

We then decided to derive temperatures from the  $H_\delta$  index. We prefer to use  $H_\delta$  because we might expect some star-to-star variation in Fe abundances. These were obtained by fitting two straight lines on the  $H_\delta - T_{\text{eff}}(\text{Fe})$  plot: one for stars with  $T_{\text{eff}}(\text{Fe}) < 8500$  K, which we called  $T_{\text{Cool}}$ , and one for stars with  $T_{\text{eff}}(\text{Fe}) > 9000$  K, which we called  $T_{\text{Hot}}$  (see Figure 6). The finally adopted temperature from  $H_\delta$  ( $T_{\text{eff}}(H_\delta)$ ) was  $T_{\text{Cool}}$  for  $T_{\text{eff}}(\text{phot}) < 8400$  K;  $T_{\text{Hot}}$  if  $T_{\text{eff}}(\text{phot}) > 9750$  K; and  $T_{\text{eff}}(H_\delta) = w * T_{\text{Cool}} + (1 - w) * T_{\text{Hot}}$  if  $8400 < T_{\text{eff}}(\text{phot}) < 9750$  K. In this last formula,  $w = (T_{\text{eff}}(\text{phot}) - 8400) / (9750 - 8400)$ . For those stars for which no  $H_\delta$  index could be derived owing to the contamination by the Th-lamp lines, we adopted  $T_{\text{eff}}(\text{phot})$  as best estimates of the effective temperatures.

Figure 8 compares  $T_{\text{eff}}(H_\delta)$  with  $T_{\text{eff}}(\text{phot})$  (as well as with temperatures from individual colours). The correlation is quite tight, with an r.m.s. of 144 K. The small residual scatter may be explained by errors in the differential reddening estimates of  $\sim 0.01$  mag, which is well within the accuracy of the method devised by Monaco et al. (2004). While such corrections appear small, there was clear improvement on the results from use of  $T_{\text{eff}}(H_\delta)$  rather than  $T_{\text{eff}}(\text{phot})$ . We hence assign an error of  $\pm 100$  K to  $T_{\text{eff}}(H_\delta)$ .

Once effective temperatures and differential reddening values were accurately determined, surface gravities  $\log g$  can be determined from the location of the stars in the colour-magnitude diagram (after correction for differential reddening) with very small errors, because masses of the stars cannot be very different from an average value of  $0.63 M_\odot$  (see Gratton et al. 2010). To this purpose, we adopted bolometric corrections from Kurucz (1992, for the metallicity of  $[\text{Fe}/\text{H}] = -1.70$  given by Harris 1996) and a distance modulus of  $(m - M)_V = 13.6$  (Harris, 1996). Surface gravities have errors not larger than  $\pm 0.05$  dex.

More critical is the derivation of microturbulent velocities  $v_t$ . For & Sneden (2010) have shown that the value of  $v_t$  changes systematically with temperature along the HB, reaching a maximum near the RR Lyrae instability strip. Quite high values of  $v_t$  are then appropriate for the cooler stars in our sample, while lower ones are more appropriate for hotter stars. Our limited spectral range - hence line list - does not in general allow derivation of reliable  $v_t$  values, so we adopted  $v_t = 3.0 \text{ km s}^{-1}$  for stars with  $T_{\text{eff}}(H_\delta) > 9000$  K, and  $v_t = 3.0 - 0.6(T_{\text{eff}}(H_\delta) - 9000)$  for cooler stars. However, in about 20% of the cases we had to modify this value, by as much as  $1.5 \text{ km s}^{-1}$  in the most extreme

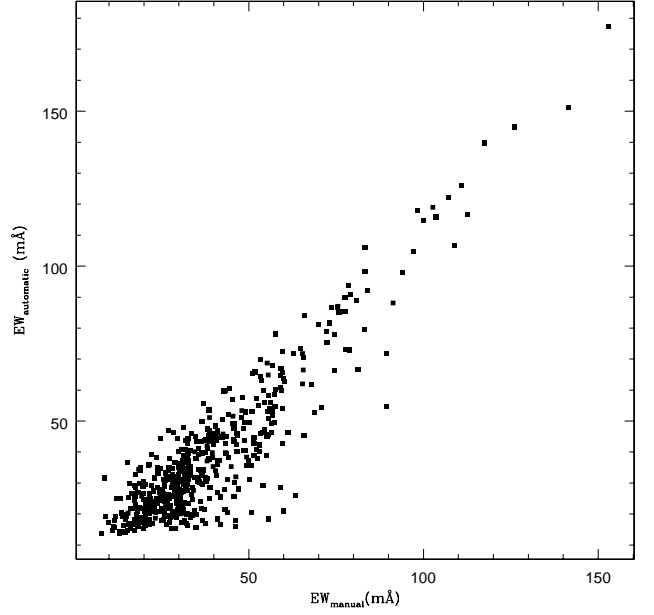


**Fig. 9.** Comparison between EWs measured manually and by the automatic procedure described in the text. The automatic EWs were corrected for the relation given in the text before being plotted.

cases, to reduce the scatter in abundances from individual lines of O I and Fe I. Errors in these estimates of  $v_t$  are quite large, so we think a value of  $\pm 1 \text{ km s}^{-1}$  is appropriate.

Finally, we adopted the same model metal abundance of  $[\text{A}/\text{H}] = -1.70$  (Harris 1996) for all stars. While M 22 is known to have a spread in  $[\text{Fe}/\text{H}]$ , this is not greater than 0.25 dex peak to valley (Marino et al. 2011b). An error bar of  $\pm 0.2$  dex should then be appropriate for  $[\text{A}/\text{H}]$ .

We may compare our estimate for temperature and gravity with Salgado et al. (2013) ones for the 14 stars in common between the two samples. On average, there are no systematic differences: the offset (in the sense ours-Salgado et al.) is  $93 \pm 117$  K (r.m.s.=436 K) for temperatures and  $0.05 \pm 0.07$  dex (r.m.s.=0.27 dex) for gravities.

### 3.2. Equivalent widths

Our abundances rest on analysis of equivalent widths (EW). They were obtained by line integration, and are the average of a manual measure, where line edges and local continuum level were set by eye inspection of the spectra, and of an automatic measure that is a measure of the average of the flux within a band four times the FWHM wide centred on the line (taking the radial velocity of the star into consideration), divided for the average fluxes in two comparison “continuum” regions (each  $\sim 2 \text{ Å}$  wide) on both sides of each line. The EWs measured with the automatic procedure were typically slightly lower than those measured manually:  $EW_{\text{Auto}} = 0.872 EW_{\text{Manual}} - 6.7 \text{ mÅ}$ , with an r.m.s. of the differences of  $9.7 \text{ mÅ}$ . The two sets of EWs were put on a uniform scale by correcting the automatic measures to the manual ones. Figure 9 compares the two sets of EWs.



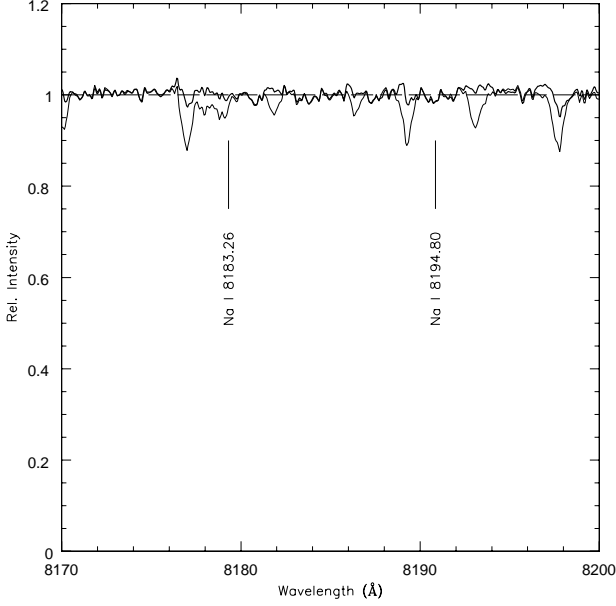


**Fig. 10.** A portion of the spectrum of star #2 including the Na I doublet at 8183-94 Å before (thin line) and after (thick line) the division for telluric lines. Dashed line is an approximate reference continuum. The Na I lines are very faint, The weakest blue line is not detected; the strongest red one is at the limit of detection.

Care was taken to consider the star-to-star variations in the widths of the lines due to stellar rotation (see previous paragraph). On the other hand, identification of local continuum and line blending are generally not a problem, since very few detectable lines are typically present. In the near infrared, subtraction telluric line subtraction is an issue for N and Na lines. It was obtained by dividing the spectra for the average of early type stars with very different radial velocities obtained throughout our programme (see Figure 10).

Using the Cayrel (1988) formula, we find that the equivalent widths have errors of  $\pm 2$ ,  $\pm 3$ , and  $\pm 5$  mÅ for HR03, HR12, and HR19A spectra, respectively. Errors are up to twice as large for rapidly rotating stars.

### 3.3. Helium abundances

Following Villanova et al. (2009), we derived He abundances for stars with an effective temperature in the range  $9000 < T_{\text{eff}} < 11000$  K from the He I line (actually a narrow multiplet) at 5875.6 Å. Figure 11 shows some examples of the He lines. To show them more clearly, we averaged spectra of different stars in bins in temperature. Figure 12 shows the run of the EW of this line with temperature for individual stars. Given the rather low S/N ( $\sim 50$ ) of the spectra and the weakness of the He line, He abundances for individual stars have quite large errors.

Marino et al. (2013b) present a non-LTE analysis of the He lines in BHB stars of NGC 2808. They also used a different code

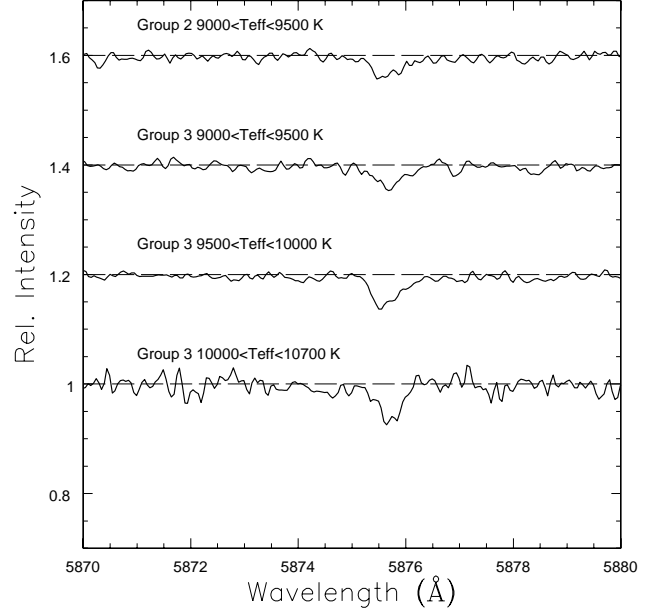


**Fig. 11.** Average spectra in the region of the He I line at 5876 Å for stars in different temperature bins. See Section 4 for the definition of different groups of stars. Spectra have been offset for clarity.

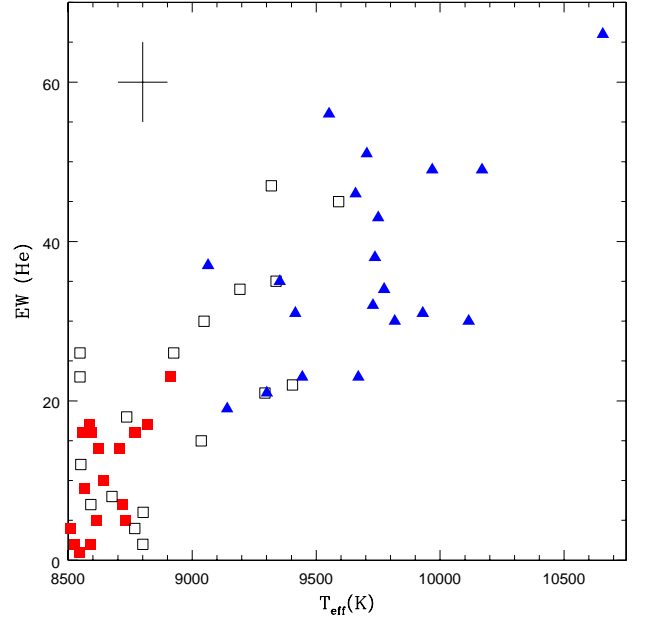


**Fig. 12.**  $T_{\text{eff}}$  vs the equivalent width of the He I line at 5876 Å. Different colours are for stars of different groups (see Section 4): Group 1: red filled squares; Group 2: black open squares; Group 3: blue filled triangles. Typical error bars are also shown.

to synthesize He lines. The average He they obtained for their stars in NGC 2808 is quite high,  $Y = 0.34 \pm 0.01 \pm 0.05$ , where the first error bar is derived from star-to-star scatter, and the second one describes the effects of systematics. Marino et al. determined an He abundance that is consistent with the one used to compute the stellar atmosphere, while in our previous anal-

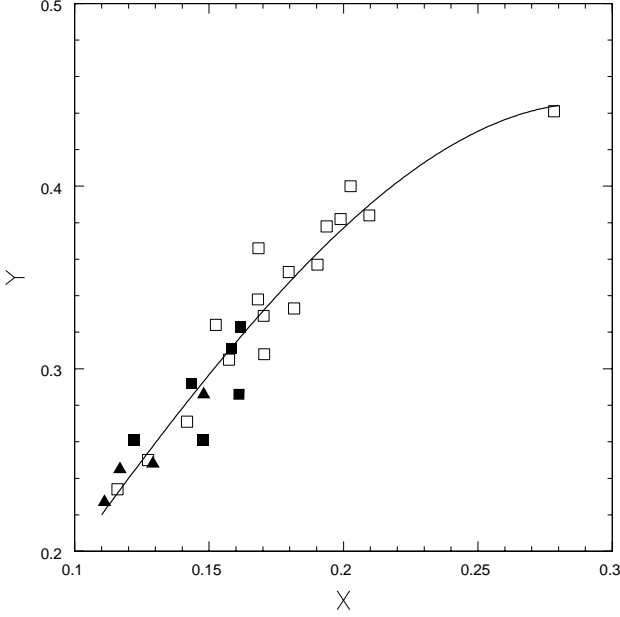


**Fig. 13.** Relation between the  $X$  index for the strength of the He I line at  $5876 \text{ \AA}$  (see Eq. (2) for a definition) and the He abundance by mass  $Y$  for BHB stars in NGC 2808 (Marino et al. 2013b: open squares), NGC 6752 (Villanova et al. 2009: filled triangles), and M 4 (Villanova et al. 2012: filled squares). He abundances from these two last papers were corrected for departures from LTE and a zero point offset of 0.036 in  $Y$ . Overimposed is the best fit cubic through the origin (Eq. (3)).

ysis we assumed He to be a tracer element; that is, the model atmosphere is assumed independently of the He abundance that is derived. Our approach may lead to (unphysical) very large He abundances when the strength of the He line is overestimated due to measuring errors. The error bar obtained using Marino et al. approach is then by far more realistic than obtained assuming it is a trace element. Furthermore, we assumed LTE, while Marino et al. compute full statistical equilibrium calculations. It appears that their methods are superior to those that we used in previous papers of this series, so it is interesting to obtain abundances on their scale.

We do not have access to their analysis code. However, we expect strong regularities in the He abundances when they are derived from the same line in a limited range of parameters, so we proceeded as follows. First, we examined the run of the non-LTE corrections. We found that these are closely related to the  $EW$  of the  $5876 \text{ \AA}$  He line and are represented well by a simple linear relation:

$$Y(\text{non-LTE}) - Y(\text{LTE}) = -9.00 \times 10^{-4} EW - 0.0192, \quad (1)$$

where the  $EW$  is in  $\text{m\AA}$ . We could correct the helium LTE abundances for NGC6752 (Villanova et al. 2009), M4 (Villanova et al. 2012) using this formula. When added to the results by Marino et al. (2013b) for NGC 2808, we thus have a consistent set of He non-LTE abundances for stars over the whole range of temperatures considered.

The He abundances for BHB stars obtained in this way are mainly a function of  $EW$  and temperature, with a small correction for surface gravity and an even smaller one for metal abun-

dance. To show this, we constructed a parameter  $X$  that is a combination of  $EW$  and temperatures:

$$X = 10^{12} EW / (T_{\text{eff}} - 5000)^{3.9}, \quad (2)$$

and then plotted the values of the He abundance by mass  $Y$  against  $X$  (see Figure 13). We found that the points display a very small scatter around a cubic fit through the origin

$$Y = 1.8224 X + 3.2125 X^2 - 14.484 X^3, \quad (3)$$

derived from stars cooler than the Grundahl jump. The r.m.s. of the points around this relation is 0.016 in  $Y$ .

We derived He abundances for M 22 stars using these relations (Column 2 of Table 6, with errors on the next column), and found an average He abundances by mass of  $Y = 0.338 \pm 0.014 \pm 0.05$ , where the first error bar is derived from star-to-star scatter, and the second one referring to systematics is simply the one adopted by Marino et al. (2013b) for NGC 2808 stars. This value is greater than expected from primordial nucleosynthesis ( $Y = 0.248$ : Cyburt 2004), even if the effect of first dredge-up is taken into account (the expected surface He enhancement is  $\Delta Y \sim 0.015$ : Sweigart 1987). This indicates that the BHB stars of M 22 hotter than 9000 K are moderately He-rich.

We notice that the He abundances of the BHB stars of M 22 are not significantly different from those of the BHB stars in the same temperature range in NGC 2808. This result could also be derived immediately by a comparison of the equivalent widths, which on average are similar at a given  $T_{\text{eff}}$ .

To verify that the high He abundances found for the BHB stars of M 22 are not simply an artefact of our procedure, we used the same approach to homogeneously determine He abundances from the  $EW$  of the  $5876 \text{ \AA}$  line for BHB stars in different clusters (see Table 7). The He abundances for NGC 1851 and M 5 we give here were derived using the formula given in this paper, and are then different from those given in our previous papers. To put these He abundances into a context, we also listed values for the metallicity and relative age of each cluster as listed by Gratton et al. (2010). We also transformed the maximum, median, and minimum colours of HB stars from the same source into minimum, median, and maximum temperature along the HB, and compared these values with the range of temperature of the stars observed in various clusters. These values are listed in Columns 4, 5, and 6 of the Table. We also listed the temperature range for the stars for which He abundances were derived. When looking at the He abundances listed in this table, it should be recalled that they do not refer to the whole cluster, but only to those HB stars that happen to be in the right temperature range ( $8500 < T_{\text{eff}} < 11500 \text{ K}$ ). Typically, there are stars hotter (and then, possibly more He-rich) and cooler (more He-poor) than the examined stars. Namely, in NGC 1851 and M 4, the stars examined by Gratton et al. (2012a) and Villanova et al. (2012) are among the hottest (and then probably He-rich) in the cluster, while in NGC 6752 they are among the coolest (and then probably He-normal) ones. In all other cases, the HB extends on both sides of the temperature range over which He abundances were determined. A correct interpretation of the result then needs a more detailed modelling for each cluster and consideration of the impact of the first dredge-up.

However, a look at this table indicates that when the observed stars are the coolest along the HB (the case of NGC 6752), we indeed recover an He abundance that is consistent within the errors with the cosmological value. As a result, systematic errors should not be large. On the other hand, there is a wide range of He abundances. In most cases, moderate He excesses with respect to the cosmological values are obtained and

are consistent with the location of stars along the HB (see e.g. the discussion by Gratton et al. 2012a and Joo & Lee 2013 for NGC 1851). The values obtained for the stars in M 22 fall at the high extreme of this range, with an average similar to that of the stars of (similar temperature) in NGC 2808. It also agrees well with the value proposed by Joo & Lee (2013) in order to explain colours of HB stars.

We conclude that while systematics errors are possibly not negligible, they should not hamper the conclusion that the BHB stars of M 22 with  $T_{\text{eff}} > 9000$  K are He-rich. We come back on this issue in Section 5.1. We notice that the He abundance we obtained for NGC 1851 is lower than what is obtained for similar stars in NGC 2808, even though the clusters have similar ages and chemical compositions. The difference is significant at about  $2\sigma$  level even; while this difference might perhaps be attributed to some other difference between stars in these clusters (e.g. different CNO/Fe ratios), we think it needs to be confirmed by more data before any strong conclusion can be drawn.

**Table 8.** Parameter for lines measured on HR03 set up

Element	Wavelength (Å)	E.P. (eV)	log $gf$
Mg I	4057.52	4.34	-0.90
Mg I	4167.22	4.34	-0.75
Si II	4128.06	9.83	0.36
Si II	4130.90	9.84	0.55
Ti II	4053.84	1.88	-1.13
Ti II	4163.61	2.58	-0.13
Ti II	4171.86	2.59	-0.29
Fe I	4046.11	1.49	0.28
Fe I	4063.60	1.56	0.06
Fe I	4071.94	1.61	-0.02
Fe I	4132.03	1.61	-0.68
Fe I	4143.88	1.56	-0.51
Fe I	4201.90	1.49	-0.71
Fe II	4173.44	2.58	-2.16
Fe II	4178.86	2.58	-2.44
Sr II	4077.91	0.00	0.15

### 3.4. Metal abundances

Abundances for other elements are given in Columns 6-16 of Table 6. As described in Gratton et al. (2011, 2012a, 2013), we obtained O abundances from the high-excitation O I triplet at 7771-74 Å and Na abundances mainly from the D resonance doublet at 5890-96 Å. For a few cool stars we could also detect the higher excitation Na I line at 8194 Å line (after appropriate correction for telluric lines). Consistently with the previous papers, abundances from these lines included non-LTE corrections following Takeda (1997) and Mashonkina et al. (2000).

As we did for NGC 1851 (Gratton et al. 2012a) and M 5 (Gratton et al. 2013), N abundances were also obtained using the high-excitation lines at 8216 and 8242 Å. Analysis of these lines also includes non-LTE corrections, following Przybilla & Butler (2001; see Gratton et al. 2012a) and appropriate correction for the contaminating telluric lines. The HR19A set up also allowed Mg abundances to be derived from the Mg II lines at 7877 and 7896 Å. Atomic parameters for all these lines were the same as used in the previous papers. Several more lines were detectable in the blue spectra provided by the HR03 set up (see

Table 8); and their oscillator strengths were taken from the NIST database.<sup>2</sup>

The use of the LTE approximation for the analysis of these elements may be questioned. For instance, Marino et al. (2013a) present both LTE and non-LTE abundances for Fe in their analysis of cool BHB stars in M 22. The non-LTE corrections were very small for Fe II ( $< 0.04$  dex, non-LTE abundances being larger) and a bit larger for Fe I (in the 0.2-0.3 dex range, non-LTE abundances being lower). When they applied these corrections, they found consistent abundances from Fe I and Fe II lines.

We found abundances from Fe I lines to be very similar to those from Fe II lines, at variance with the results by Marino et al. (2013a). This is not due to differences in temperatures and gravities, which are quite similar in the two analyses; it might rather be due to our adopting much higher values for the microturbulent velocity, because the Fe I lines we used in our analysis are typically stronger than the Fe II lines. Since microturbulent velocities are not derived from first principles, but simply modified in such a way as to obtain agreement between abundances derived from lines of different strength, and since non-LTE corrections are expected to be larger for stronger lines, it is difficult to separate the two effects. Practically speaking, in this case an LTE analysis with a high microturbulence produces abundances similar to a non-LTE analysis with lower microturbulence. Regardless the reason, we find that applying non-LTE corrections as large as those considered by Marino et al. (2013) would destroy the agreement we obtain between Fe I and II abundances, so we prefer not to apply them.

Abundances from the Sr II line at 4077 Å do not include any correction for the increased opacity due to the wings of H $\delta$ ; however, we checked that such a correction is very small ( $\leq 0.01$  dex). Furthermore, no correction for departures from LTE was applied. The size and even the sign of these corrections are not clear. Dworetsky et al. (2008) suggest that they should be small, if any, for population I A-type stars. Similar results have been obtained from statistical equilibrium calculations (Mashonkina et al. 2007; Andrievsky et al. 2011; Bergemann et al. 2012; Hansen et al. 2013) for Sr II lines in metal-poor stars, but these results are only available for  $T_{\text{eff}} < 6400$  K, that is for stars much cooler than our programme stars, and small trends are present at the high-temperature, low-gravity extreme of the range of parameters explored in these papers. The abundances of Sr that we obtain are smaller by about 0.5 dex than those by Marino et al. (2012) for subgiants in M 22. The reason for this systematic offset is not clear. On one hand, we notice that the result by Marino et al. is obtained from spectra with moderate dispersion and should then be considered with some caution, their main focus being on the difference obtained for the two SGB branches rather than on the absolute values. On the other hand, we notice that For and Sneden (2010) have obtained a low [Sr/Fe] abundance ratio (on average [Sr/Fe]=-0.30) for field BHB stars from an LTE analysis similar to ours for M 22. The stars they considered have effective temperatures and metal abundances similar to those of the stars we are analysing in M 22, and they adopted similar values for the microturbulent velocities. An even lower abundance of [Sr/Fe]=-0.7 was obtained by Ambika et al. (2004) for a supra-BHB star in M 13. This might suggest a trend toward underestimating Sr abundances in LTE analysis of low-gravity hot stars that might represent an extrapolation of the small trend observed in cooler stars by Andrievsky et al. (2013). Appropriate statistical equilibrium calculations are required to settle this point. However, the effect is

<sup>2</sup> [http://physics.nist.gov/PhysRefData/ASD/lines\\_form.html](http://physics.nist.gov/PhysRefData/ASD/lines_form.html)

not overwhelmingly strong, and we think that our LTE Sr abundances can still be used to separate different groups of stars in M 22 and to internally compare production of elements through the various  $n$ -capture processes.

**Table 9.** Sensitivity of abundances on the atmospheric parameters and total errors

Element	$T_{\text{eff}}$ (K)	$\log g$	$v_t$ (km s $^{-1}$ )	[A/H]	$EW$ (mÅ)	Total
Error	100	0.05	1.0	0.2	5	
Cool BHB star ( $T_{\text{eff}} \sim 8000$ K)						
[Fe/H] I	0.084	-0.006	-0.070	0.004	0.060	0.13
[Fe/H] II	0.029	0.013	-0.025	0.004	0.070	0.08
[N/Fe] I	-0.068	0.006	0.038	-0.004	0.113	0.14
[O/Fe] I	-0.006	0.000	-0.164	-0.011	0.064	0.18
[Na/Fe] I	0.033	-0.013	-0.010	0.001	0.119	0.12
[Mg/Fe] I	-0.001	-0.010	0.038	0.003	0.111	0.12
[Mg/Fe] II	-0.054	0.002	0.034	-0.004	0.153	0.17
[Si/Fe] II	-0.098	0.010	0.022	-0.007	0.044	0.11
[Ti/Fe] II	-0.025	0.010	0.026	-0.000	0.061	0.07
[Sr/Fe] II	0.030	0.002	0.000	0.002	0.143	0.15
Hot BHB star ( $T_{\text{eff}} \sim 10000$ K)						
He Y(NLTE)	-0.022	0.013	-0.011	-0.011	0.034	0.05
[Fe/H] I	0.061	-0.017	-0.006	0.009	0.097	0.12
[N/Fe] I	0.013	0.017	-0.010	-0.006	0.075	0.08
[O/Fe] I	0.009	0.018	-0.123	-0.012	0.038	0.13
[Na/Fe] I	0.044	0.000	-0.009	-0.003	0.062	0.08
[Mg/Fe] II	-0.016	0.026	-0.025	-0.009	0.100	0.11
[Si/Fe] II	-0.008	0.035	-0.034	-0.012	0.089	0.10

### 3.5. Sensitivity of abundances on the atmospheric parameters

The sensitivity of abundances on the adopted values for the atmospheric parameters is given in Table 9. It was obtained as usual by changing each parameter separately and repeating analysis of the abundances. We also considered the contribution to the error due to uncertainties in the equivalent widths, divided by the square root of the typical number of lines used in the analysis. The values were computed for typical uncertainties in each parameter, as determined in Section 3.1. Results are given for two stars (#1 and #129) at the extremes of the observed range of temperatures.

Results for He are for the abundance by mass  $Y$  and for the simulated non-LTE analysis of Section 3.3. For the other elements, typical uncertainties in the abundances are  $\pm 0.1$ – $0.2$  dex. In most cases, equivalent widths contribute significantly to final errors. Fe abundances are also affected by errors in the effective temperatures. Since abundances of N I, Mg II, and Si II are not influenced much by temperature for the cooler HB stars, the ratios to Fe abundances have an opposite temperature dependence. Oxygen and, in less measure, Fe abundances are also sensitive to the adopted value for the microturbulent velocity.

**Table 10.** Average parameters for the three groups

Parameter	Group 1	r.m.s.	Group 2	r.m.s.	Group 3	r.m.s.
$T_{\text{eff}}$ (K)	8468	237	8860	367	9697	372
$Y$	..	..	0.363	0.076	0.328	0.072
$< [\text{Fe}/\text{H}] >$	-1.87	0.13	-1.83	0.15	-1.63	0.13
[Sr/Fe] II	-0.54	0.26	-0.54	0.26	-0.18	0.36
[N/Fe] I	0.68	0.15	1.11	0.12	1.06	0.07
[O/Fe] I	0.65	0.12	0.54	0.16	0.54	0.23
[Na/Fe] I	-0.08	0.11	0.20	0.16	0.40	0.17
[Mg/Fe] I	0.73	0.19	0.72	0.11		
[Mg/Fe] II	0.48	0.29	0.59	0.26	0.27	0.31
[Si/Fe] II	0.48	0.19	0.56	0.23	0.32	0.20
[Ti/Fe] II	0.35	0.15	0.43	0.17	0.51	0.15

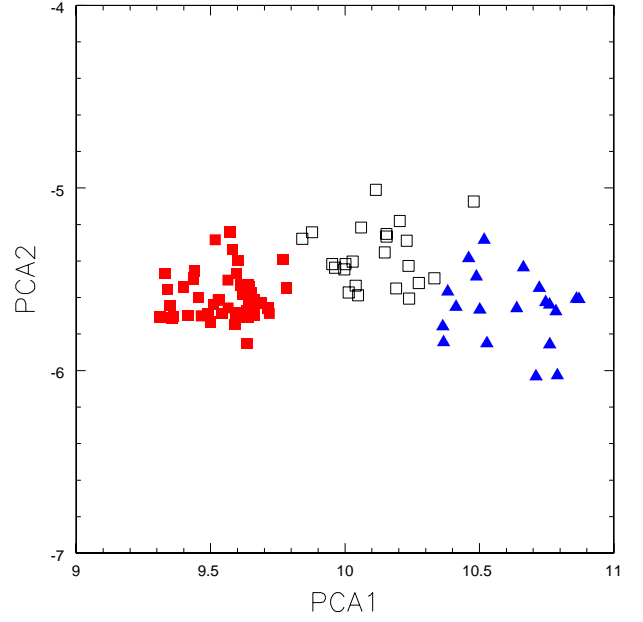


**Fig. 14.** Subdivision of the stars among the three groups in the two principal components plane. Group 1 stars are represented by red filled squares, group 2 stars by open black squares, and group 3 stars by blue filled triangles.

## 4. Cluster analysis and identifications of the main populations

Previous work on M 22 has shown that there are several different populations in this GC. Marino et al. (2009, 2011) find two main populations, each one with a different metal content. These two populations can be well discerned along the RGB and the SGB (see also Marino et al. 2012). Each one of these main populations displays a spread over the Na-O anti-correlation, showing that they have a fine structure (see Marino et al. 2011). Understanding the HB of M 22 requires identifying the progeny of these different populations during the He-core burning phase. To this purpose we should first remember that we did not observe all HB stars in our study. It is then probable that our sample does not represent the whole cluster population.

Our approach was then to identify natural groups among the observed stars. This was done using a statistical cluster analysis. We used the  $k$ -means algorithm (Steinhaus 1956; MacQueen 1967) as implemented in the  $R$  statistical package ( $R$  Development Core Team 2011), where  $R$  is a system for statisti-

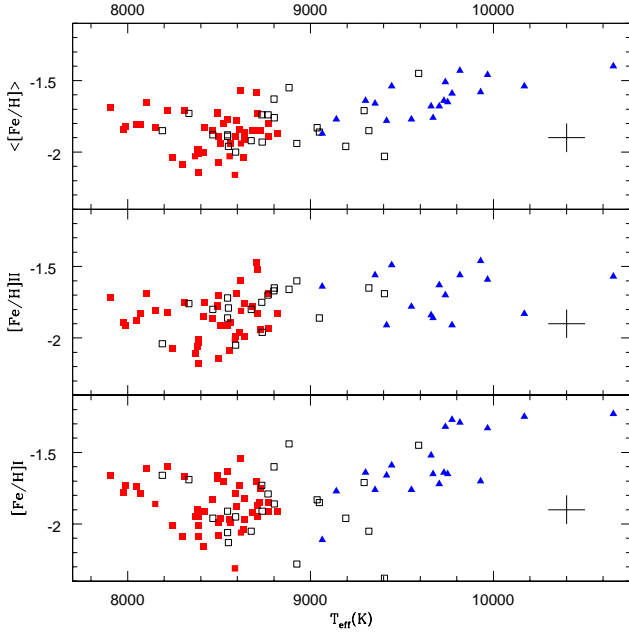


**Fig. 15.**  $T_{\text{eff}}$  vs the abundances from Fe I (lower panel), Fe II lines (upper left panel, and the average of the two values (upper right panel). Different colours are for stars of different groups (see Section 4). Group 1: red filled squares; Group 2: black open squares; Group 3: blue filled triangles. Typical error bars are also shown.

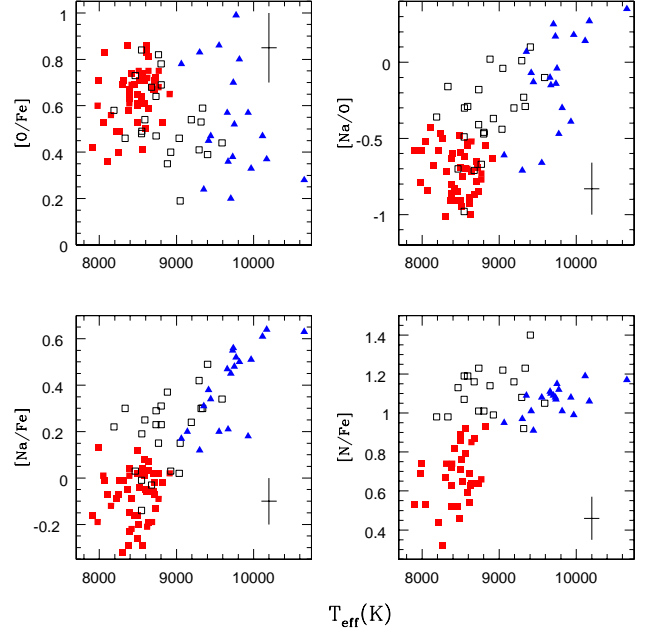


**Fig. 16.**  $T_{\text{eff}}$  vs the abundances of N (lower right panel), Na (lower left panel), and O (upper right panel) and the [Na/O] abundance ratio (upper left panel). Different colours are for stars of different groups (see Section 4). Group 1: red filled squares; Group 2: black open squares; Group 3: blue filled triangles. Typical error bars are also shown.

cal computation and graphics, freely available on-line<sup>3</sup>. The following parameters were considered when performing the analysis: effective temperatures (to avoid a variance that is too dissimilar to those of other quantities, we used  $T_{\text{eff}}/10000$  K in the analysis) and absolute visual magnitude  $M_V$ , which describe the location of stars along the HB; and four parameters describing the chemical composition of the stars ( $\langle [\text{Fe}/\text{H}] \rangle$ ,  $[\text{N}/\text{H}]$ ,  $[\text{O}/\text{H}]$ ,  $[\text{Na}/\text{H}]$ ). The first parameters are related to the main subdivisions in metal-poor and metal-rich populations, which are discernible from photometry of the SGB and RGB (Marino et al. 2009, 2012), while the three remaining ones are related to the Na-O anti-correlation.

We found that a subdivision in three groups is able to capture a large fraction of the information, the variance between groups representing 66.7 % of the total variance. The three groups are made of 49, 23, and 20 stars. Figure 14 shows the subdivision of the stars into the three groups on the plane of the two principal components. A principal component analysis is the first step of a statistical cluster analysis. The two principal components are defined as follows:

$$\text{PCA1} = 1.11 \cdot 10^{-5} T_{\text{eff}} + 0.151 M_V + 0.209 \log n(\text{Fe}) \\ + 0.068 \log n(\text{O}) + 0.656 \log n(\text{Na}) + 0.697 \log n(\text{N})$$

and

$$\text{PCA2} = -4.70 \cdot 10^{-6} T_{\text{eff}} - 0.262 M_V - 0.340 \log n(\text{Fe}) \\ - 0.738 \log n(\text{O}) - 0.238 \log n(\text{Na}) + 0.461 \log n(\text{N})$$

The main parameters of the three groups are listed in Table 10. The r.m.s. for the abundances of the individual groups

agree well with the scatter expected for uncertainties in the analysis listed in the last column of Table 9, in agreement with expectations if these groups have a physical meaning. The main driver for the subdivision into these groups is the correlated variations in N and Na abundance, which are responsible for most of the variations in PCA1, and PCA2 is a combination of several parameters with more weight on N and O abundances. Figure 14 shows that the subdivision into groups is driven by PCA1. This means that the subdivision in groups is mainly based on the chemistry. Figures 15 and 16 give the run of the abundances of Fe, Na, N, O with effective temperature, with different symbols for the three groups. The separation is quite evident. Figure 17 gives the same run for the sum of N and O abundances with temperature. The subdivision into groups is still clear. We notice that effective temperature plays a minor role in the definition of PCA1. That there is quite a clear segregation of the groups in the colour-magnitude diagram is essentially a consequence of the fact that stars with different chemistry occupy different locations along the horizontal branch. Finally, Figure 18 compares the Na-O anti-correlation found for the HB stars observed in this paper with the one obtained for the RGB by Marino et al. (2011a).

From this data, we found that Groups 1 and 2 are made of metal-poor stars. Abundances for these HB stars match the abundances found by Marino et al. (2011) very well for their metal-poor population, and this can be identified with the b-SGB population. We obtained low Sr abundances for these two groups, again in good agreement with the result by Marino et al. The two groups also differ for N and Na abundance, the first group being poorer in these elements than the second one. The low abundances of N and Na of the first group are compatible with the one for evolved metal-poor giants in the field (see e.g. Gratton et al. 2000). These stars can then be identified with the first (or primordial) population in the cluster. This group is also slightly

<sup>3</sup> <http://www.R-project.org>

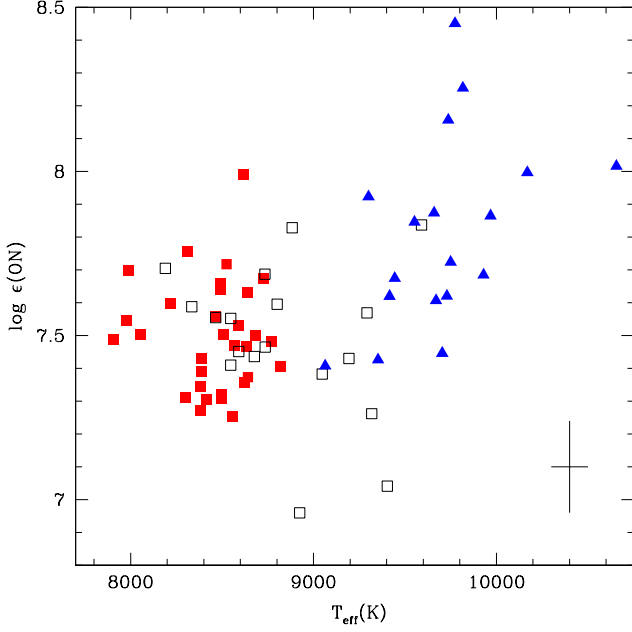


**Fig. 17.**  $T_{\text{eff}}$  vs the sum of N and O abundances. Different colours are for stars of different groups (see Section 4). Group 1: red filled squares; Group 2: black open squares; Group 3: blue filled triangles.

more O-rich than the second one; however, we did not find any extreme O-poor stars in our sample, while some of them were found by Marino et al. (2011b). We then think that the second group is made of stars that have an intermediate position along the Na-O anti-correlation and that stars strongly depleted in O are not sampled in our analysis because they fall in the region of the HB hotter than the Grundahl jump.

Group 3 is made up of metal-rich stars. Again, the abundances match those found by Marino et al. (2011b) very well for this group of stars, which can be identified with the f-SGB population. We notice that this group is rich in Sr, as found by Marino et al. (2012) for the f-SGB stars of M 22 (although there is an offset between the Sr abundances we obtain for HB stars and those found by Marino et al. for SGB stars; see Section 3.4). This group of stars is rich in Na and N, but it is also quite rich in O. We think they can be identified with the less O-poor/Na-rich stars along the Na-O anti-correlation for the metal-rich stars of Marino et al. (2011b). As for the metal-poor stars, Marino et al. (2011b) also find evidence for a metal-rich population strongly depleted in O and very rich in Na. Again, we think that this population is not sampled by our analysis because these stars also fall in the HB-region that is hotter than the Grundahl jump.

We finally notice that stars of both Groups 2 and 3 seem overabundant in He. The result for Group 2 is more uncertain, because it is based on only eight stars that, being not very hot, have quite weak He lines (see Figure 11). The result for Group 3 is more robust, since it is based on 20 stars that have stronger He lines. However, in both cases the internal scatter is not much larger than expected for the errors listed in Table 9. We then suggest that stars in both these groups are overabundant in He with respect to the cosmological value.

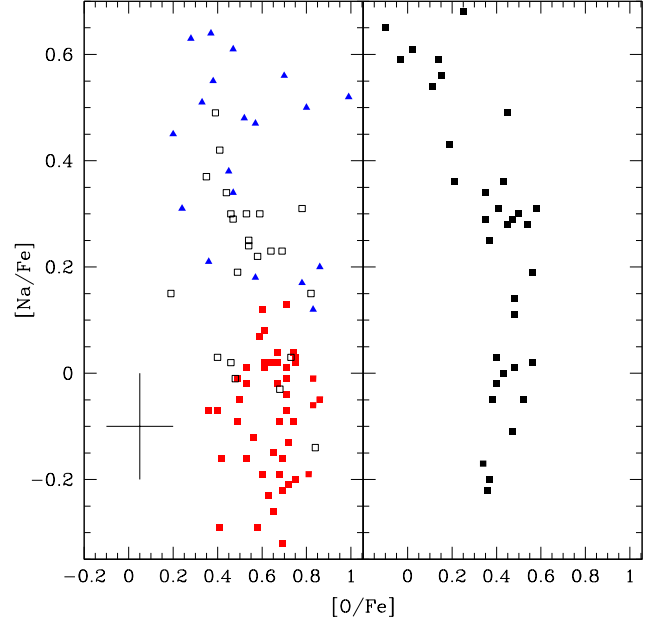


**Fig. 18.**  $[O/Fe]$  vs  $[Na/Fe]$  for BHB stars (left panel) and RGB stars from Marino et al. (2011a: right panel). In the left panel different colours are for stars of different groups (see Section 4). Group 1: red filled squares; Group 2: black open squares; Group 3: blue filled triangles. Typical error bars for our analysis are also shown.

**Table 11.** Number of stars of different populations of M 22: FG=first generation with primordial composition (normal He, low Na, high O); SG-I=second generation with intermediate composition (moderately high He and Na, moderately low O); SG-E=second generation with extreme characteristics (very high He and Na, very low O)

Population	FG	SG-I	SG-E	Total
RGB: Marino et al. (2011a)				
Metal-poor	12	4	5	21
Metal-Rich	-	9	5	14
Frequency over the RGB and SGB (Marino et al. 2011a, 2011b)				
Metal-poor	0.34	0.11	0.14	0.60
Metal-rich	-	0.26	0.14	0.40
BHB: This paper				
Metal-poor	49	23	-	72
Metal-rich	-	20	-	20
Frequency over the whole HB				
Metal-poor	0.39	0.15	~0.14	~0.68
Metal-rich	-	>0.14	~0.14	~0.32

## 5. Discussion

We intend to make a quantitative comparison between the observed distribution of stars along the HB of M 22 and appropriate synthetic colour-magnitude diagrams, in order to shed light on the properties of the different stellar populations of M 22. This comparison makes use of rough estimates of the frequencies of these different populations that were derived as follows.

First, we recall that our observations are biased because we observe neither the stars hotter than the Grundahl jump nor those



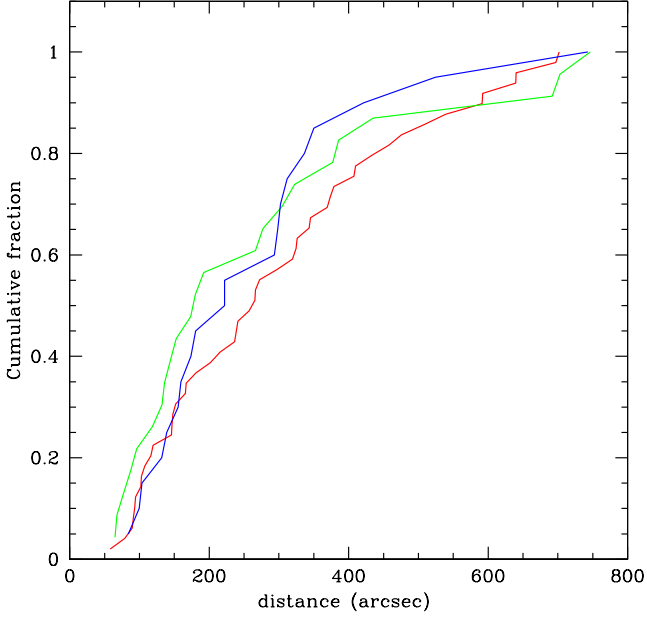


**Fig. 19.** Cumulative distribution of stars in different groups with separation from cluster centre. Different colours are for stars of different groups (see Section 4): Group 1: red; Group 2: green; Group 3: blue

in the RR Lyrae instability strip. Owing to the possible presence of radial gradients, it would be important to sample different cluster regions. In fact, Kunder et al. (2013) find a clear indication that stars on the f-SGB are more centrally concentrated than those on the b-SGB in M 22. They did not find any clear trend for HB stars, but in that case their analysis was only limited to the annulus from 4 to 6 arcmin from the centre and a limited number of stars; for reference, the half-light radius of M 22 is 3.36 arcmin according to Harris (1996), and gradients are expected to be clearest when a wide range in logarithm of distance from centre is considered. For practical reasons (avoiding collisions of fibres and contamination by neighbours), most of our stars are at rather large distances from the cluster centre, within an annulus from 1 to 12.5 arcmin, with a median value of 4.0 arcmin. Figure 19 shows that Group 1 looks somewhat less concentrated than Groups 2 and 3. This would agree with expectations and with the result on the SGB by Kunder et al. (2013), because stars of the first generation are usually less concentrated than those of the second generation, and we identified Group 1 with the first generation. However, Kolmogorov-Smirnov tests show that differences between groups are not significant, probably because we only observed a few stars in each group. Since the effect is not overwhelming, we neglect radial variations in this discussion.

We then considered the statistics of different groups of stars from the analysis of Marino et al. (2011a). While there are only 35 stars in this sample, there are not strong evolutionary biases because stars with slightly different chemical compositions end up in similar locations along the RGB. They may then give a rough idea of the real frequencies of the main populations. Furthermore, as discussed in the previous section, abundances by Marino et al. (2011a) are on a scale that looks quite similar to what we obtain for the HB stars, so that a direct comparison is possible. Table 11 provides the results of these counts. In this table, FG are O-rich, Na-poor stars that we attribute to the first

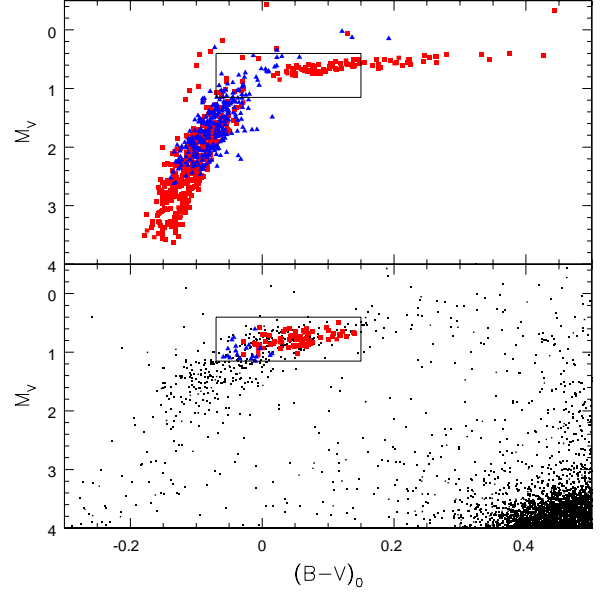


**Fig. 20.** Comparison between a synthetic (upper panel) and an observed (lower panel) colour-magnitude diagram for the horizontal branch of M22. Red squares are metal-poor stars (in the lower panel, stars of Groups 1 and 2); blue triangles are metal-rich stars (in the lower panel, stars of Group 3). In the lower panel, stars not observed in this paper are dots. The region of the HB observed in this paper is marked with a rectangle in both panels

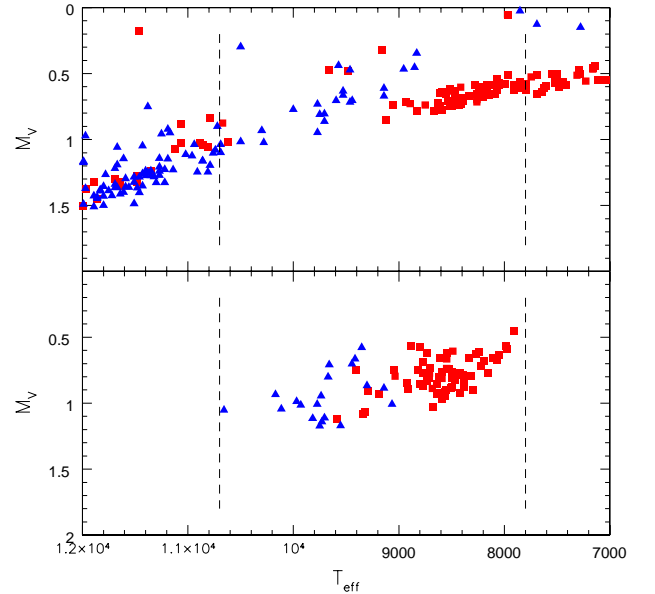


**Fig. 21.** Details of the comparison between synthetic (upper panel) and observed (lower panel)  $T_{\text{eff}} - M_V$  diagram for the horizontal branch of M22. Red squares are metal-poor stars (in the lower panel, stars of groups 1 and 2); blue triangles are metal-rich stars (in the lower panel, stars of group 3). The region of the HB observed in this paper is within the dashed lines in both panels

generation of stars in M 22, and SG-I and SG-E are second generation with intermediate or extreme values for Na and O abundances throughout the Na-O anti-correlation (see Carretta et al. 2009).

The FG stars are expected to have a He abundance close to the cosmological value; SG-I and SG-E are expected to be moderately and extremely He-rich stars. We then identified our Group 1 with the FG metal-poor population, Group 2 with the SG-I metal-poor population, and Group 3 with the SG-I metal-rich population found on the RGB using data by Marino et al. (2011a).

Using the photometry by Richter et al. (1999), which covers a region within 5 arcmin of the cluster centre with a median of 2.6 arcmin, we found that in their data there are 71 stars hotter than the Grundahl jump (that is, 32% of the total HB stars), 16 stars (7%) in the instability strip, and 138 (61%) stars within the range of temperatures observed by us. These values are consistent with the star counts in the HB by Kunder et al. (2013).

If we make the assumption that stars in the instability strip are the cooler extension of our Group 1, in agreement with the properties of the RR Lyrae in M 22 (Kunder et al. 2013), and are then FG metal-poor stars, we obtain that a fraction of  $0.07 + 0.61 \times (49/92) = 0.39$  of the HB stars of M 22 belongs to this population. Within the rather large errors due to small number statistics, this frequency agrees with the one found for this population along the RGB by Marino et al. (2011a). We also note that this group seems to coincide with the group that is redder than the gap at about 9000-9500 K noticed by Kunder et al. (2013) and that makes up 39% of the HB stars of their sample.

We further assume that all SG-I metal-poor stars have temperatures within the range we observed. This is justified by the fact that we do not have any group 2 star close to edge of this range. In this case the frequency of metal-poor SG-I stars in the whole HB can be obtained by multiplying the frequency in our sample by the fraction of HB stars that are within the temperature range within our sample, that is,  $0.61 \times (23/92) = 0.15$ .

If we repeat a similar estimate for the SG-I metal-rich stars (identified with our Group 3), we get a fraction of  $0.61 \times (20/92) = 0.13$ . However, this may be considered more a lower limit than real data, because we may have missed stars of this group because they are slightly hotter than the temperature limit of our survey. This is also suggested by a comparison with the results by Kunder et al. (2013): our intermediate groups (including both Groups 2 and 3) seem in fact to coincide with the clump of stars at the HB position parameter  $l_{\text{HB}} \sim 26$  in their analysis, which includes some 35-40% of the HB stars of M 22. This is more than the fraction of 0.28 we obtain by summing the stars in our Groups 2 and 3. Also, there are stars in this clump that are clearly hotter and fainter than the stars we observed.

On the other hand, we missed all SG-E stars that make up 28% of the stars along the RGB observed by Marino et al. (2011a). They very likely end up on the HB with temperatures hotter than the Grundahl jump, which are 32% of total according to the Strömgren photometry by Richter et al. (1999). According to Marino et al. (2011a), these hot stars should be roughly equally divided among the metal-poor and the metal-rich populations.

With these assumptions, we obtain the frequencies given in the last part of Table 11. These values should be considered with caution, because they are based on low number statistics. However, on the whole they suggest that some 60-70% of the HB stars of M 22 belong to the metal-poor population and 30-40% to the metal rich one. Given the large uncertainties, these values cannot be considered to disagree with the overall 60-40

subdivision found by Marino et al. (2011a) from RGB stars and a similar rough estimate for SGB stars by Marino et al. (2011b). We notice that a 70-30 subdivision has also been obtained recently by Carretta et al. (2014, in preparation) who consider the bimodal distribution into two sequences along the RGB in the  $(y, v - y)$  colours from Richter et al. (1999) photometry, and by Joo & Lee (2013) from a re-analysis of ground-based photometric data by Lee et al. (2009) and of HST-ACS data by Piotto (2009).

We note, in summary:

- All Group 1 stars (roughly 39% of the cluster stars, with 7% cooler than the blue edge of the instability strip) are cooler than 8900 K. They should then have a very narrow mass range, since all are more massive than  $0.64 M_{\odot}$ . For the stars we observed (hotter than the instability strip), the range in mass is from  $0.66$  to  $0.64 M_{\odot}$ . They should have either all the same He abundance, essentially the cosmological value, or a very narrow range (less than 0.01 in  $Y$ ).
- Group 2 stars (roughly 15% of the cluster stars) also have a limited range in temperature ( $8300 < T_{\text{eff}} < 9600$  K), which indicates a very limited range in mass too:  $0.63 < M < 0.65 M_{\odot}$ . They therefore are likely to all have nearly the same He abundances at  $Y \sim 0.015$  larger than Group 1 stars. This value is lower than indicated by the strength of the 5876 Å line.
- All Group 3 stars (roughly 18% of the cluster stars) are hotter than 9000 K. Those stars that we observed are also cooler than 10700 K; however, there should be hotter stars in this group, up to  $\sim 12000$  K. Depending on the CNO content, this sets an upper limit to the mass, but there should also be a narrow range around it, suggesting a unique value for He abundance. For normal [CNO/Fe], this means  $0.60 < M < 0.62 M_{\odot}$  and  $Y \sim 0.28$ , and for CNO enhanced, this means a range in mass  $0.57 < M < 0.59 M_{\odot}$  and  $Y \sim 0.30$ . Again, this value is lower than indicated by the strength of the 5876 Å line, though the discrepancy is not as large as found for Group 2 stars if CNO is enhanced.
- In addition, there should also be more He-rich stars in M 22, not observed by us because hotter than 10700 K. They should make up about 28% of the cluster. Using photometry by Kunder et al. (2013), we found that half of them are hotter than 14000 K, that is, less massive than  $\sim 0.54 M_{\odot}$ . These stars should be very rich in He ( $Y > 0.33$ ). The other half should have  $10700 < T_{\text{eff}} < 12000$  K, and a He abundance of  $Y \sim 0.30$ .

Based on the previous discussion, we prepared synthetic colour-magnitude diagrams for the HB of M 22. They were performed as described in Salaris et al. (2008) and Dalessandro et al. (2011). We employed the HB evolutionary tracks for [Fe/H]=-1.8 as reference set for the metal-poor stars, and [Fe/H]=-1.6 for the metal-rich ones from the BaSTI database (Pietrinferni et al. 2006). In addition, we have interpolated among the  $\alpha$ -enhanced BaSTI models to determine HB tracks for various values of the helium content  $Y$ . Finally, we also considered both the reference set and the CNONa anti-correlated models with CNO sum enhanced by 0.3 dex (Pietrinferni et al. 2009). We adopted a distance modulus  $(m-M)_V=13.60$  and  $E(B-V)=0.36$  from Harris (1996).

In our simulations, we have considered as constraints a number ratio between bright (metal-poor) and faint (metal-rich) SGB stars equal to 60:40. We notice that reproduction of the exact details of the colour/temperature distribution requires a lot of fine

tuning on the exact parameters. This fine tuning is very time expensive and possibly misleading, because it might lead to over-confidence on details that may instead depend on the way models were constructed. We then focussed on the main features of such a comparison. We made several attempts to fit both the HB and the other sequences in M 22 (RGB and SGB), changing mass loss and the range of He abundances for the various populations. We find that continuous distributions in He cannot reproduce the segregation between the three groups of stars observed along the HB of M 22. Furthermore, the minimum He abundance of metal-rich stars should be greater than the cosmological value, or else these stars would be fainter (at same temperature) than metal-poor stars, which is not indicated by observations. We then finally assumed the following recipe for the different populations of M 22:

- Metal poor: two subcomponents, the first one (corresponding to Group 1) has a uniform distribution of He in the narrow range  $0.246 < Y < 0.251$  and a total average mass lost along the RGB of  $0.16 M_{\odot}$ , with a Gaussian distribution with an r.m.s. of  $0.01 M_{\odot}$ ; and a second one (whose cooler part corresponds to Group 2) has a uniform distribution of He in the narrow range  $0.285 < Y < 0.319$  and the same total average mass loss of Group 1, but with a narrow Gaussian distribution with an r.m.s. of  $0.005 M_{\odot}$
- Metal rich: a uniform He distribution over the range  $0.285 < Y < 0.325$  and a Gaussian distributed total mass loss with average value of  $0.160 M_{\odot}$  and r.m.s. of  $0.005 M_{\odot}$

We assumed for both the metal-poor and metal-rich HB stellar components an RGB progenitor whose age at the RGB tip is equal to 12 Gyr. Finally, a differential reddening of 0.05 mag (see Kunder et al. 2013) was added to the synthetic data.

We had to assume values of  $Y$  that are actually lower than determined from our spectroscopic data for the He-rich populations. In fact, if HB stars were even richer in He than assumed in the models, they would be brighter than observed. Also, we would expect them to be less massive and bluer than observed if they were coeval and lost the same amount of mass along the RGB than the He-normal stars. We conclude that while there is good qualitative agreement between these different helium abundances, there is some disagreement about the exact quantitative level, which is only partly surprising if we consider that they are derived by using completely different and independent techniques.

Figures 20 and 21 compare the synthetic HBs with the observed ones. We notice that this simulation reproduces (i) the ratios between stars within the RR Lyrae instability strip, blueward of it with  $M_V < 16$ , and in the blue tail, i.e.  $M_V > 16$  measured by Kunder et al. (2013), within Poisson errors; (ii) the number ratio between metal-poor and metal-rich stars within the region considered in this paper; (iii) roughly, the segregation of the stars of different groups in the  $T_{\text{eff}} - M_V$  plane observed in this paper; (iv) the average He abundance of metal-rich stars in the range of effective temperature observed in this paper (the actual value of  $Y=0.29$  is at the lower limit of the range admitted by our data); and the number ratio of metal poor/metal rich stars measured on the SGB by Marino et al. (2009). The scatter in the observed diagram of Figure 20 looks larger than for theoretical colours. This is largely due to residual photometric errors or some underestimate of the impact of differential reddening. In fact, if we look at the distribution of stars with temperatures of Figure 21 (where the impact of photometric error and differential reddening is much smaller), the agreement between observation and models is improved.

Answering a question from the referee, we noticed that the scatter in  $M_V$  around the mean  $T_{\text{eff}} - M_V$  relation ( $\sim 0.10$  mag) is larger than predicted from evolutionary effects ( $\sim 0.07$  mag) for the metal-poor stars, while it is actually smaller than predicted (0.15 vs 0.18 mag) for the metal-rich ones. The residual errors in differential reddening ( $\sim 0.01$  mag in  $E(B-V)$ ), that is,  $\sim 0.05$  mag in the residuals in  $M_V$ ) may explain a part of the larger-than-expected scatter observed for metal-poor stars. Also, errors due to photometry should be considered. Finally, it is possible that the assumptions we made in our population synthesis represents an over-simplification of the real situation in M 22. However, we stress that our comparison only gives a sketch of the real properties of the populations in M 22.

On the whole, this interpretation of the HB of M 22 agrees with what is proposed by Joo & Lee (2013). Details are slightly different, because we find that there should be some overlap between the most He-rich stars of the metal-poor population and the moderately He-rich stars of the metal-rich one. Such fine detailing is only possible here because we have determined the chemical composition of individual stars, while Joo & Lee could only work with photometric data. But excluding this detail, the agreement between ours and their description of the HB of M 22 is impressive.

## 6. Conclusions

We presented a spectroscopic abundance analysis of a sample of 92 blue HB stars in M 22 in order to discuss the relation existing between chemical composition and the location of the stars along the HB of globular clusters. The stars selected for the analysis are in a restricted range of temperatures between 7800 and 10700 K. Cooler stars were not considered because they are RR Lyrae variables, while surface abundances for hotter stars are known to be heavily affected by microscopic diffusion and radiative levitation. However, stars in our sample are representative of the majority of HB stars in this clusters. We obtained spectra in three spectral ranges, including the stronger lines of Na and O and of the  $n$ -capture element Sr. In addition, we were able to derive abundances for He, N, and Fe (from both neutral and singly ionized lines), as well as for other species (Mg, Si, and Ti). Whenever possible, reddening free effective temperatures were obtained from a calibration of the strength of  $H\delta$ ; otherwise they were obtained from visual and violet colours. Abundances of Na, O, N, and He include non-LTE corrections obtained from literature calibrations. We did not apply non-LTE corrections to Fe abundances because we get agreement between Fe I and Fe II abundances when assuming LTE. This might be a consequence of the rather high values we adopted for the microturbulent velocity, which do, however, agree with determinations for field BHB stars. We get a rather high value for the He abundance, similar to the one recently obtained for similar stars in NGC 2808 by Marino et al. (2013b), but higher than in other GCs for which a similar analysis was performed.

We then applied a statistical cluster analysis to our data and found that the stars we studied divide into three groups that occupy adjacent location along the HB, with some overlap. The coolest group is metal-poor, Sr-poor, N- and Na-poor, and O-rich. This result confirms an earlier finding for a few stars by Marino et al. (2013a). The intermediate group is still metal-poor and Sr-poor, but is N- and Na-rich, and moderately O-poor. The hotter group is metal-rich and Sr-rich, moderately N- and Na-rich, but also O-rich. These three groups have a clear correspondence with the different populations found on the RGB and SGB by Marino et al. (2011b, 2012): the metal-poor and  $s$ -poor pop-

ulation that is also found along the RGB that is the progeny of the b-SGB, and the metal-rich and *s*-rich RGB one that is the progeny of the f-SGB. We do not find any extremely O-poor star in our sample, but HB stars with this composition are expected to be hotter than the range we observed. Our result then nicely confirms and extends previous investigations and supports the assumption that the spread in colour of HB stars within a GC is mainly determined by variations in the chemical composition, as measured by proxies like Na and O and whenever possible, directly by He lines. We also found that there is not only qualitative agreement between predictions of this scenario and observations, but also a quantitative one; furthermore, star counts in different evolutionary phases agree with each other, supporting the proposed relation between different groups of HB, RGB, and SGB stars.

We found that there should be fairly He-rich stars in M 22, with  $Y \sim 0.32$  or even larger, in agreement with what recently proposed by Joo & Lee (2013). These stars should be traceable on the MS of the cluster, once adequate photometric data is available.

Finally, we found several fast rotators. They are concentrated in a narrow region of the HB, with  $8400 < T_{\text{eff}} < 9400$  K. There is strong correlation between rotational velocity and temperature within our Group 1, which might suggest that fast rotators (where surface rotation is assumed to be a proxy for core rotation, that is the parameter that might be linked to position on the HB) are less massive than slow rotators, as proposed many years ago by Peterson et al. (1983). However, first, the difference in mass is very small ( $\leq 0.015 M_{\odot}$ ), so that core rotation is much less important than chemical composition. Second, there is not any similar correlation between temperature and rotational velocity for stars in the other groups. This seems to instead indicate that surface rotation can only be observed in a restricted range of temperatures along the HB of globular clusters. While the lack of significant rotation in cooler stars might be explained by their larger radius and by magnetic braking, we have not an explanation for the slow rotation of the hotter stars (see, however, Vink and Cassisi 2002 for a potential scenario). Further investigation is required to establish that core rotation is indeed related to the colour of HB stars.

**Acknowledgements.** This publication makes use of data products from the Two Micron All Sky Survey, which is a joint project of the University of Massachusetts and the Infrared Processing and Analysis Center/California Institute of Technology, funded by the National Aeronautics and Space Administration and the National Science Foundation. This research has made use of the NASA's Astrophysical Data System. This research has been funded by PRIN INAF "Formation and Early Evolution of Massive Star Clusters". We thank Philipp Richter for sending us the Strömgren photometric data they obtained for M 22. VD is an ARC Super Science Fellow. We thank an anonymous referee for suggestions that helped to improve the paper.

## References

- Ambika, S., Parthasarathy, M., Aoki, W., et al. 2004, *A&A*, 417, 293  
 Andrievsky, S.M., Spite, F., Korotin, S.A., et al. 2011, *A&A*, 530, 105  
 Bedin, L.R., Piotto, G., Anderson, J., et al. 2004, *ApJ*, 605, L125  
 Behr, B.B., Cohen, J.G., McCarthy, J.K., Djorgovski, S.G. 1999, *ApJ*, 517, L135  
 Behr, B.C., Djorgovski, S.G., Cohen, J.G., et al. 2000a, *ApJ*, 528, 849  
 Behr, B.C., Cohen, J.G., McCarthy, J.K. 2000b, *ApJ*, 531, L37  
 Bergemann, M., Hansen, C.J., Bautista, M., Ruchti, G. 2012, *A&A*, 546, 90  
 Carretta, E., Recio-Blanco, A., Gratton, R.G., Piotto, G., Bragaglia, A. 2007, *ApJ*, 671, L125  
 Carretta, E., Gratton, R.G., Lucatello, S., et al. 2010, *ApJ*, 722, L1  
 Carretta, E., Lucatello, S., Gratton, R.G., Bragaglia, A., D'Orazi, V. 2011, *A&A*, 533, A69  
 Cassisi, S., Salaris, M., Irwin, A.W. 2003, *ApJ*, 588, 862  
 Catelan, M. 2009, Resolved Stellar Populations, ASP Conference Series, D. Valls-Gabaud and M. Chavez eds, *Ap&SS*, 320, 261  
 Cayrel, R. 1988 in *The Impact of Very High S/N Spectroscopy on Stellar Physics*, IAU Symp 132, eds. G. Cayrel de Strobel and M. Spite, Kluwer Academic Publishers, Dordrecht, p.345  
 Cyburt, R.H. 2004, *Phys. Rev. D*, 70, 023505  
 Da Costa, G.S., Held, E.V., Saviane, I., Gullieuszik, M. 2009, *ApJ*, 705, 1481  
 Dalessandro, E., Salaris, M., Ferraro, F.R., et al. 2011, *MNRAS* 410, 694  
 D'Antona, F., Bellazzini, M., Caloi, V., et al. 2005, *ApJ*, 631, 868  
 Dotter, A., 2013, *MSAIt*, 84, 97  
 Dworetsky, M.M., Dyer, A., Persaud, J.L. 2008, *Contrib. Astron. Obs. Skalnaté Pleso* 38, 141  
 Faulkner, J. 1966, *ApJ*, 144, 978  
 For, B.-Q., Sneden, C., 2010, *AJ*, 140, 1694  
 Fusi Pecci, F., Bellazzini, M. 1997, in *The Third Conference on Faint Blue Stars*, Eds. Philip, A.G.D., Liebert, J., Saffer, R.A., Davis, Schenectady, p. 255  
 Gratton, R., Sneden, C., 1987, *A&A*, 178, 179  
 Gratton, R., Sneden, C., Carretta, E., Bragaglia, A. 2000, *A&A*, 354, 169  
 Gratton, R.G., Carretta, E., Bragaglia, A., Lucatello, S., D'Orazi, V. 2010, *A&A*, 517, 81  
 Gratton, R.G., Lucatello, S., Carretta, E., et al. 2011, *A&A*, 534, 123  
 Gratton, R.G., Lucatello, S., Carretta, E., et al., 2012a, *A&A*, 539, 19  
 Gratton, R.G., Villanova, S., Lucatello, S., et al. 2012b, *A&A*, 544, 12  
 Gratton, R.G., Lucatello, S., Sollima, A., et al. 2013, *A&A*, 549, 41  
 Grundahl, F., Catelan, M., Landsman, W.B., Stetson, P.B., Andersen, M.I. 1999, *ApJ*, 524, 242  
 Hansen, C.J., Bergemann, M., Cescutti, G. et al. 2013, *A&A*, 551, 57  
 Harris, W.E. 1996, *AJ*, 112, 1487  
 Iben, I.Jr. 1968, *Nature*, 220, 143  
 Joo, S.-J., Lee, J.-W., 2013, *ApJ*, 762, 36  
 Kaluzny, J., Thompson, I.B. 2001, *A&A*, 373, 899  
 Kunder, A., Stetson, P.B., Cassisi, S., et al. 2013, *AJ*, 146, 119  
 Kurucz, R.L. 1993, CD-ROM 13, Smithsonian Astrophysical Observatory, Cambridge  
 Lee, J.-W., Kang, Y.-W., Lee, J., & Lee, Y.-W. 2009, *Natur*, 462, 480  
 Lovisi, L., Mucciarelli, A., Lanzoni, B., et al. 2012, *ApJ*, 754, L91  
 MacQueen, J.B. 1967, *Mathematical Statistics and Probability* (University of California Press), 281  
 Marino, A.F., Milone, A.P., Piotto, G. et al. 2009, *A&A*, 505, 1099  
 Marino, A.F., Villanova, S., Milone, A.P., et al. 2011a, *ApJ*, 730, L16  
 Marino, A.F., Sneden, C., Kraft, R.P. et al. 2011b, *A&A*, 532, 8  
 Marino, A.F., Milone, A.P., Sneden, C., et al. 2012, *A&A*, 514, 15  
 Marino, A.F., Milone, A.P., Lind, K. 2013a, *ApJ*, 768, 27  
 Marino, A.F., Milone, A.P., Przybilla, N., et al. 2013b *MNRAS*, in press (arXiv1310.4527)  
 Mashonkina, I.I., Shimanskii, V.V., Sakhibullin, N.A. 2000, *Astron. Rep.* 44, 790  
 Mashonkina, L.I., Vinogradova, A.B., Ptitsyn, D.A., Khokhlova, V.S., Chernetsova, T.A. 2007, *Astron. Rep.* 51, 903  
 Milone, A.P., Stetson, P.B., Piotto, G., et al. 2009, *A&A*, 503, 755  
 Moehler, S. 2001, *PASP*, 113, 1162  
 Monaco, L., Pancino, E., Ferraro, F.R., Bellazzini, M. 2004, *MNRAS*, 349, 1278  
 Moni Bidin, C., Moehler, S., Piotto, G., et al. 2006, *A&A*, 451, 499  
 Munari, U., Sordo, R., Castelli, F., Zwitter, T. 2005, *A&A*, 442, 1127  
 Norris, J., Cottrell, P.L., Freeman, K.C., Da Costa, G.S. 1981, *ApJ*, 244, 205  
 Norris, J., 2004, *ApJ*, 612, L25  
 Pasquini, L., Castillo, R., Dekker, H. et al. 2004, *SPIE*, 5492, 136  
 Peterson, R., *ApJ*, 1983, 275, 737  
 Peterson, R.C., Rood, R.T., Crocker, D.A. 1995, *ApJ*, 453, 214  
 Pietrinferni, A., Cassisi, S., Salaris, M., et al. 2009, *ApJ*, 697, 275  
 Piotto, G. 2009, in *IAU Symp. 258, The Ages of Stars*, eds. E.E. Mamajek, D.R. Soderblom, & R.F.G. Wyse (Cambridge: Cambridge Univ. Press), 233  
 Piotto, G., Villanova, S., Bedin, L.R., et al. 2005, *ApJ*, 621, 777  
 Przybilla, N., Butler, K. 2001, *A&A* 379, 955  
 R Development Core Team 2011, *R: A language and environment for statistical computing*, Vienna, Austria, ISBN 3-900051-07-0  
 Recio-Blanco, A., Piotto, G., Aparicio, A., Renzini, A. 2004, *A&A*, 417, 597  
 Recio-Blanco, A., Aparicio, A., Piotto, G., De Angeli, F., & Djorgovski, S.G. 2006, *A&A*, 452, 875  
 Richter, P., Hilker, M., Richtler, T. 1999, *A&A*, 350, 476  
 Rood, R.T. 1973, *ApJ*, 184, 815 A.G.D., Hayes, D.S., IAU Coll. 68 L. Davis Press, Schenectady, p. 369  
 Salaris, M., Rieello, M., Cassisi, S., Piotto, G. 2004, *A&A*, 420, 911  
 Salaris, M., Cassisi, S., Pietrinferni, A. 2008, *ApJ*, 678, L25  
 Salgado, C., Moni Bidin, C., Villanova, S., Geisler, D., Catelan, M. 2013, *A&A*, 559, A101  
 Sandage, A., Wallerstein, G. 1960, *ApJ*, 131, 598  
 Sandage, A., Wildey, R. 1967, *ApJ*, 150, 469  
 Skrutskie, M.F., Cutri, R.M., Stiening, R., et al. 2006, *AJ*, 131, 1163  
 Steinhaus, H. 1956, *Bull. Acad. Polon. Sci.*, 4, 801  
 Sweigart, A.V., 1987, *ApJS*, 65, 955

- Takeda, Y. 1997, PASJ, 49, 471  
van den Bergh, S. 1967, AJ, 72, 70  
Villanova, S., Piotto, G., Gratton, R.G. 2009, A&A, 499, 755  
Villanova, S., Geisler, D., Piotto, G., Gratton, R.G., 2012 ApJ, 748, 62  
Ventura, P., D'Antona, F., Mazzitelli, I., Gratton, R. 2001, ApJ, 550, L65  
Vink, J.S., Cassisi, S., 2002, A&A, 392, 553

**Table 3.** Photometric data (only available in electronic form)

Star	RA (J2000)	Dec (J2000)	V	err	B	err	I	err	K	y	b	v	E(B-V)
1	18 36 28.032	-24 00 26.56	14.090	0.006	14.509	0.006	13.451	0.008	12.677				0.304
2	18 37 03.597	-23 58 10.33	14.182	0.006	14.638	0.008	13.483	0.008	12.884				0.359
4	18 35 57.058	-24 04 02.93	14.171	0.006	14.494	0.006	13.613	0.007	12.225				0.327
5	18 36 27.299	-23 51 44.57	14.204	0.006	14.530	0.008	13.732	0.006	13.268	14.160	14.419	14.702	0.337
7	18 36 20.968	-24 05 59.01	14.193	0.006	14.587	0.006	13.558	0.006	12.943				0.327
8	18 36 27.716	-23 52 30.85	14.213	0.007	14.590	0.006	13.669	0.007		14.184	14.453	14.765	0.342
10	18 36 20.551	-23 58 39.19	14.202	0.006	14.540	0.006	13.688	0.007	13.112	14.133	14.427	14.733	0.297
11	18 36 31.111	-23 51 45.13	14.262	0.006	14.678	0.006	13.667	0.007	13.200	14.226	14.535	14.878	0.352
12	18 37 08.735	-23 57 16.79	14.327	0.006	14.810	0.006	13.627	0.008	12.921				0.355
13	18 36 22.368	-23 59 42.69	14.226	0.006	14.627	0.006	13.629	0.008	12.989				0.301
14	18 36 32.388	-23 49 35.53	14.292	0.006	14.634	0.006	13.796	0.008	13.100	14.255	14.533	14.804	0.338
15	18 36 16.730	-23 58 14.50	14.231	0.007	14.634	0.007	13.683	0.007					0.340
16	18 36 29.247	-23 57 02.07	14.240	0.007	14.614	0.007	13.742	0.007	12.914	14.152	14.452	14.779	0.341
17	18 36 07.706	-23 55 43.39	14.247	0.007	14.644	0.007	13.566	0.014	12.776	14.139	14.477	14.846	0.346
18	18 36 29.351	-24 00 28.56	14.238	0.006	14.619	0.006	13.655	0.006	13.053				0.304
20	18 36 18.877	-23 56 48.84	14.250	0.006	14.711	0.006	13.593	0.007	12.804	14.167	14.535	14.909	0.339
21	18 36 34.560	-23 54 35.57	14.266	0.007	14.759	0.006	13.580	0.007	12.676	14.170	14.549	14.932	0.354
23	18 36 20.369	-23 53 05.12	14.288	0.006	14.777	0.007	13.617	0.009	12.757				0.349
24	18 36 21.337	-23 55 03.24	14.277	0.008	14.746	0.009	13.647	0.018					0.360
25	18 36 32.170	-23 53 01.18	14.292	0.007	14.688	0.007	13.744	0.010	12.981	14.210	14.532	14.861	0.346
26	18 36 16.749	-23 53 50.95	14.298	0.006	14.770	0.006	13.598	0.006		14.256	14.621	15.012	0.354
29	18 36 37.359	-23 59 56.05	14.278	0.006	14.623	0.007	13.739	0.007	13.072				0.294
31	18 36 20.332	-23 59 37.93	14.283	0.006	14.661	0.006	13.714	0.006	13.113				0.307
33	18 35 55.275	-24 03 53.28	14.302	0.006	14.604	0.006	13.741	0.007					0.301
34	18 36 17.938	-23 55 00.89	14.309	0.006	14.777	0.007	13.630	0.009	12.884	14.226	14.595	14.991	0.349
35	18 36 12.781	-23 55 38.98	14.314	0.006	14.683	0.006	13.755	0.007		14.258	14.543	14.884	0.324
38	18 36 10.313	-23 59 35.76	14.312	0.006	14.620	0.008	13.785	0.007	13.051				0.297
39	18 36 30.809	-23 54 25.39	14.331	0.006	14.736	0.006	13.741	0.009		14.267	14.581	14.929	0.362
40	18 36 09.803	-23 55 13.11	14.339	0.006	14.743	0.008	13.739	0.007	13.102	14.265	14.577	14.935	0.346
41	18 36 23.753	-23 50 15.98	14.384	0.006	14.781	0.006	13.802	0.006	13.100	14.351	14.650	14.970	0.336
42	18 36 37.681	-23 57 24.37	14.334	0.006	14.760	0.006	13.701	0.008	12.884	14.280	14.622	14.983	0.319
43	18 36 02.427	-23 53 38.28	14.355	0.006	14.780	0.006	13.696	0.006	12.938	14.301	14.648	15.027	0.336
45	18 35 50.826	-23 55 14.43	14.350	0.006	14.739	0.008	13.740	0.007	13.032				0.336
46	18 36 54.722	-23 56 02.12	14.416	0.006	14.777	0.006	13.855	0.007	13.056				0.343
47	18 36 18.200	-23 57 44.95	14.347	0.006	14.655	0.006	13.869	0.007	13.350	14.274	14.550	14.838	0.351
48	18 36 36.443	-23 51 34.51	14.387	0.006	14.822	0.008	13.784	0.007	13.117	14.348	14.671	15.007	0.335
50	18 36 21.568	-23 55 28.85	14.370	0.006	14.791	0.006	13.768	0.007	12.983	14.318	14.649	15.012	0.353
51	18 36 34.273	-23 49 31.01	14.430	0.006	14.846	0.006	13.830	0.007	13.341				0.339
52	18 36 23.316	-23 58 54.13	14.369	0.006	14.703	0.008	13.856	0.007	13.308	14.320	14.591	14.900	0.307
54	18 36 26.414	-23 55 41.96	14.379	0.006	14.842	0.007	13.750	0.007	12.859	14.314	14.666	15.034	0.350
55	18 36 19.075	-23 53 16.95	14.400	0.006	14.821	0.008	13.817	0.007	12.925				0.349
56	18 35 55.361	-23 48 07.38	14.459	0.006	14.795	0.006	13.889	0.006	13.311				0.347
60	18 36 13.546	-23 53 37.28	14.407	0.008	14.813	0.007	13.883	0.007	12.826				0.347
61	18 36 13.299	-24 02 24.02	14.388	0.006	14.730	0.006	13.857	0.007	13.395				0.301
62	18 36 15.560	-23 57 27.25	14.389	0.006	14.684	0.006	13.913	0.006	13.336	14.329	14.584	14.867	0.341
63	18 36 20.844	-23 56 57.59	14.391	0.006	14.784	0.006	13.829	0.007	13.143	14.320	14.649	14.983	0.341
67	18 36 13.521	-23 55 08.17	14.410	0.006	14.761	0.006	13.854	0.007	13.642	14.339	14.637	14.977	0.346
68	18 36 38.183	-23 48 19.48	14.478	0.006	14.869	0.008	13.893	0.007	13.404				0.339
69	18 36 23.533	-23 56 04.66	14.408	0.007	14.817	0.007	13.858	0.007	12.942	14.331	14.642	14.988	0.339
70	18 36 50.837	-23 58 04.35	14.472	0.006	14.879	0.006	13.877	0.007	13.201				0.343
72	18 36 25.842	-23 51 06.89	14.454	0.006	14.817	0.008	13.952	0.007	13.018	14.419	14.694	14.996	0.346
73	18 35 51.258	-23 51 37.71	14.449	0.006	14.858	0.006	13.783	0.006	13.068				0.336
76	18 35 38.506	-23 59 41.47	14.415	0.006	14.714	0.006	13.890	0.006	13.446				0.327
77	18 36 40.999	-23 58 31.27	14.484	0.006	14.890	0.006	13.896	0.007	13.241				0.343
79	18 35 41.235	-23 55 44.50	14.427	0.006	14.790	0.008	13.825	0.007	13.271				0.336
80	18 36 24.876	-23 56 42.30	14.430	0.006	14.811	0.006	13.884	0.007	13.405	14.384	14.681	15.002	0.351
81	18 36 01.511	-23 51 44.26	14.470	0.006	14.893	0.006	13.828	0.007	13.266				0.352
83	18 37 17.808	-23 52 31.58	14.575	0.006	14.924	0.008	14.043	0.007	13.589				0.355
84	18 36 26.252	-23 53 17.37	14.463	0.006	14.861	0.008	13.876	0.007	10.745	14.423	14.724	15.062	0.334
87	18 35 41.848	-23 49 41.49	14.515	0.006	14.856	0.006	13.922	0.006	13.400				0.347
88	18 36 18.315	-23 54 17.71	14.472	0.007	14.813	0.007	13.968	0.008	14.490				0.351
89	18 35 57.467	-23 47 59.08	14.539	0.007	14.834	0.008	14.085	0.009	13.520				0.347
90	18 36 31.690	-23 55 11.47	14.471	0.006	14.891	0.006	13.871	0.007		14.435	14.769	15.116	0.350
91	18 36 17.798	-23 55 37.53	14.470	0.006	14.819	0.006	13.946	0.007	13.776	14.416	14.699	15.027	0.353
92	18 36 07.048	-23 51 54.35	14.500	0.006	14.909	0.006	13.835	0.006	13.361	14.435	14.763	15.113	0.341
94	18 36 21.227	-23 49 07.40	14.533	0.006	14.882	0.006	14.051	0.007	13.610	14.514	14.788	15.079	0.352
95	18 36 23.529	-23 52 33.80	14.496	0.006	14.820	0.008	14.016	0.007	14.313	14.458	14.709	14.991	0.364
96	18 36 26.039	-23 56 26.15	14.473	0.006	14.827	0.006	13.962	0.007	13.505	14.429	14.721	15.019	0.341
98	18 36 41.823	-23 56 01.35	14.486	0.006	14.874	0.007	13.878	0.006	13.347	14.433	14.740	15.086	0.341
100	18 36 10.753	-23 58 14.26	14.479	0.008	14.810	0.007	14.036	0.007					0.351
102	18 36 40.999	-23 58 31.27	14.484	0.006	14.887	0.008	13.847	0.008					0.343
104	18 36 26.957	-23 55 11.11	14.499	0.006	14.889	0.006	13.939	0.007	13.331	14.450	14.745	15.066	0.341
105	18 36 29.377	-23 53 11.04	14.532	0.007	14.854	0.007	14.075	0.009		14.468	14.727	15.016	0.346
106	18 36 21.457	-23 57 50.18	14.519	0.006	14.882	0.006	13.983	0.007	13.406	14.461	14.770	15.081	0.323
107	18 36 28.185	-23 56 29.13	14.528	0.006	14.870	0.008	14.035	0.007		14.481	14.744	15.032	0.341
108	18 36 30.649	-23 54 44.72	14.541	0.006	14.926	0.006	13.976	0.007	12.999	14.502	14.794	15.121	0.358
110	18 36 47.542	-23 55 49.88	14.623	0.007	14.981	0.007	14.120	0.007	13.398				0.343
111	18 36 28.419	-23 49 00.28	14.624	0.006	15.016	0.006	14.091	0.007	13.345				0.338
112	18 36 44.423	-23 52 52.92	14.644	0.006	14.958	0.008	14.159	0.007	13.669				0.352
113	18 36 11.463	-23 58 26.56	14.578	0.006	14.835	0.008	14.148	0.007					0.297
115	18 36 54.324	-23 53 15.40	14.680	0.006	14.973	0.006	14.201						



**Table 4.** S/N of spectra, radial velocities, FWHM, and rotational velocities (only available in electronic form)

Star	S/N(3)	S/N(12)	S/N(19)	RV(3) (km s <sup>-1</sup> )	RV(12) (km s <sup>-1</sup> )	RV(19) (km s <sup>-1</sup> )	<RV> (km s <sup>-1</sup> )	r.m.s. (km s <sup>-1</sup> )	FWHM(3) (km s <sup>-1</sup> )	FWHM(12) (km s <sup>-1</sup> )	FWHM(19) (km s <sup>-1</sup> )	<FWHM> (km s <sup>-1</sup> )	rms (km s <sup>-1</sup> )	$v \sin i$ (km s <sup>-1</sup> )
1	45	75	50	-153.5	-153.2	-154.6	-153.8	0.8	21.8	18.8	22.7	21.6	2.0	7
2	67	54	62	-149.0	-142.3	-144.7	-145.3	3.4	27.7	19.5	23.6	25.4	4.1	12
4	30	40	43	-155.5	-149.8	-156.2	-153.8	3.5	18.7	26.3	24.9	21.5	4.0	7
5	45	64	49	-136.1	-138.7	-136.7	-137.2	1.4	35.1	18.9	26.5	30.3	8.1	17
7	41	50	50	-157.9	-152.9	-157.5	-156.1	2.8	28.2	27.8	21.8	26.3	3.6	13
8	69	80	65	-134.4	-130.4	-132.5	-132.4	2.0	27.6	15.2	17.0	22.8	6.7	9
10	53	50	49	-141.8	-144.4	-141.0	-142.4	1.8	41.0	55.1	46.6	44.6	7.1	29
11	57	54	55	-143.1	-143.4	-144.9	-143.8	1.0	30.5	43.0	40.8	35.2	6.7	21
12	50	55	44	-152.6	-148.4	-153.6	-151.5	2.7	28.8	33.6	36.0	31.6	3.7	18
13	42	52	51	-147.1	-149.2	-147.8	-148.0	1.1	24.9	38.7	27.4	27.6	7.3	14
14	54	50	54	-140.9	-141.4	-143.9	-142.0	1.6	17.7	21.2	21.6	19.3	2.1	<5
15	56	69	51	-139.8	-137.2	-140.1	-139.1	1.6	21.9	21.2	18.2	20.8	2.0	6
16	31	45	61	-141.9	-153.4	-143.0	-146.1	6.4	18.9	27.8	17.5	19.8	5.6	<5
17		68	65		-136.7	-130.7	-133.7	4.2		24.6	32.3	29.8	5.5	16
18	50	59	50	-137.1	-142.2	-140.8	-140.0	2.6	18.4	19.2	27.6	21.1	5.1	7
20	52	68	63	-152.4	-149.9	-148.6	-150.3	2.0	27.0	31.5	20.4	25.7	5.6	12
21	35	56	62	-138.7	-137.4	-139.7	-138.6	1.2	21.3	25.4	19.3	21.4	3.5	7
23	52	68	63	-147.9	-142.4	-145.1	-145.1	2.7	33.9	28.7	32.1	32.7	2.6	19
24	56	60	38	-143.4	-141.8	-147.0	-144.1	2.7	33.6	23.4	30.8	31.3	5.3	18
25	36	61	43	-132.7	-135.2	-133.8	-133.9	1.2	28.7	17.6	18.4	24.2	6.2	11
26	42	61	60	-157.5	-151.8	-155.4	-154.9	2.9	26.2	24.9	24.8	25.6	0.8	12
29	49	58	56	-149.3	-147.7	-149.2	-148.7	0.9	37.3	35.9	33.4	36.0	2.0	22
31	46	51	51	-152.0	-153.3	-154.1	-153.1	1.0	27.2	23.0	24.8	25.9	2.1	12
33	29	42	37	-148.9	-150.8	-157.2	-152.3	4.4		62.0	57.9	25.4	2.9	12
34	58	53	46	-148.2	-147.6	-146.9	-147.5	0.7	31.7	28.9	34.5	32.1	2.8	18
35	59	53	53	-151.8	-149.5	-150.1	-150.5	1.2	27.4	28.5	24.6	26.8	2.0	13
38	57	54	46	-157.7	-154.4	-154.3	-155.5	1.9	31.0	28.1	27.3	29.6	2.0	16
39	34	45	48	-126.0	-138.0	-125.4	-129.8	7.1	49.6	31.8	47.0	46.3	9.6	30
40	43	60	60	-154.2	-145.3	-150.4	-150.0	4.5	18.7	21.6	24.2	20.7	2.8	6
41	49	49	66	-151.3	-146.1	-150.7	-149.4	2.9	19.2	17.8	23.3	20.2	2.9	5
42	36	51	40	-138.1	-137.3	-135.9	-137.1	1.1	33.0	23.6	23.9	29.1	5.4	16
43	60	68	56	-150.5	-148.3	-150.3	-149.7	1.2	22.3	30.2	20.5	22.9	5.1	9
45	48	49	54	-155.5	-148.3	-153.4	-152.4	3.7	38.5	30.3	34.0	36.0	4.1	22
46	51	55	51	-153.2	-151.1	-152.8	-152.4	1.1	24.2	28.9	20.3	23.8	4.3	10
47	52	51	48	-140.4	-148.5	-144.5	-144.5	4.0	34.2	35.1	38.0	35.4	2.0	21
48	47	57	67	-131.4		-139.6	-135.5	5.7	34.5	26.1	37.4	34.2	5.9	20
50	50	54	46	-140.7	-140.7	-137.5	-139.6	1.9	29.8	34.2	22.0	28.2	6.1	15
51	37	52	62	-134.7	-145.0	-133.0	-137.5	6.5	45.1	33.5	28.3	38.6	8.6	24
52	44	42	56	-150.9	-150.1	-146.8	-149.3	2.2	75.0		63.8	72.8	7.9	50
54	44	50	63	-150.4	-144.0	-155.5	-150.0	5.7	59.9	42.9	41.3	52.1	10.3	34
55	53	55	62	-141.5	-146.3	-140.2	-142.7	3.2	37.9	51.1	36.3	39.3	8.1	24
56	33			-146.0		-150.5	-148.2	3.2	35.0			35.0		21
60	69	56	51	-175.0	-168.7	-168.5	-170.7	3.7	25.9		16.3	22.7	6.8	9
61	46	51	52	-145.8	-146.1	-146.2	-146.0	0.2	49.2	51.6	34.0	45.2	9.6	29
62	55	63	25	-147.9	-149.0	-160.5	-152.5	7.0	39.1	35.3	47.4	41.0	6.2	26
63	56	63	44	-147.7	-147.9	-144.7	-146.8	1.8	23.6	27.5	28.2	25.5	2.5	12
67	47	47	57	-140.9	-147.2	-139.7	-142.6	4.0	44.8	39.3	30.6	39.9	7.2	25
68	37	46	33	-141.6	-144.1	-139.2	-141.6	2.5	19.3	37.8	23.7	23.2	9.7	9
69	45	56	44	-174.3	-162.1	-175.3	-170.6	7.4	34.7	23.7	26.0	30.6	5.8	17
70	55	56	40	-151.5	-148.6	-149.5	-149.9	1.4	28.3	29.8	24.4	27.4	2.8	14
72	45	52	59	-140.1	-140.3	-137.9	-139.4	1.3	67.3		45.6	60.0	15.4	40
73	44	50	41	-148.6	-142.8	-142.1	-144.5	3.6	35.8	23.6	41.4	35.7	9.1	21
76	38	48	56	-133.2	-152.7	-137.3	-141.1	10.3	50.2		50.1	50.2	0.1	33
77	52	56	45	-154.7	-148.6	-154.2	-152.5	3.4	29.6	33.3	24.7	28.7	4.3	15
79	55	50	41	-155.1	-152.3	-164.6	-157.4	6.5	50.9	32.3	52.5	48.7	11.2	32
80	43	53	58	-141.1	-146.6	-134.5	-140.7	6.1	62.9		60.1	62.0	2.0	42
81	47	47	52	-143.3	-141.9	-143.1	-142.7	0.8	21.9	33.6	32.1	26.5	6.4	13
83	34	44	39	-150.8	-141.7	-143.0	-145.2	4.9	26.0	19.9	20.9	23.7	3.3	10
84	35	51	60	-153.7	-150.2	-154.6	-152.8	2.3	36.1	46.0	34.5	37.0	6.2	22
87		46	55			-140.0	-140.0			54.5		54.5		36
88	52	56	43	-155.9	-149.1	-144.2	-149.7	5.9	48.0	36.7	38.7	43.7	6.1	28
89	35	41	48	-139.8	-145.8	-146.3	-144.0	3.6	22.2	13.5	17.5	19.6	4.3	<5
90	28	50	46	-144.0	-156.3	-146.2	-148.8	6.6	54.8	54.8	45.0	52.0	5.6	34
91	62	66	46	-130.7	-137.0	-129.8	-132.5	3.9	53.1	63.0	58.1	56.0	4.9	37
92	27	37	36	-143.7	-148.5	-139.1	-143.8	4.7	36.1	49.8	38.5	38.7	7.3	24
94	57	49	53	-143.4	-144.5	-144.6	-144.2	0.6	19.0	19.0	13.4	17.4	3.3	<5
95	37	51	42	-135.2	-144.1	-137.2	-138.8	4.7	21.0	24.5	18.2	20.7	3.2	6
96	54	59	54	-147.1		-147.5	-147.3	0.3	41.9		29.1	37.6	9.0	23
98	32	48	53	-148.2		-150.4	-149.3	1.6	37.6		27.2	34.2	7.4	20
100	49	50	49	-132.3	-133.5	-137.2	-134.3	2.5	21.6	23.5	20.4	21.5	1.6	7
102	40	57	39	-164.6	-161.4	-161.8	-162.6	1.8	29.6	23.4	15.8	24.8	7.0	11
104	50	58	41	-160.2	-160.4	-158.1	-159.6	1.3	33.8	24.1	29.8	31.3	4.9	18
105	36	49	43	-150.0	-140.3	-144.9	-145.1	4.9	38.8	37.7	39.9	38.9	1.1	24
106	52	40	32	-146.7	-148.4	-154.4	-149.8	4.0	66.7	50.4	72.8	66.1	11.6	45
107	40	43	44	-147.1	-143.3	-142.5	-144.3	2.4		47.7	42.7	44.4	3.5	28
108	50	53	38	-160.2	-151.9	-158.5	-156.9	4.4	59.3	60.8	42.1	54.6	10.4	36
110	29	47	37	-139.3	-137.4	-143.2	-140.0	3.0	19.0	28.3	20.3	20.7	5.0	6
111	39	36	49	-134.6	-144.7	-141.2	-140.2	5.1		45.9	62.4	56.9	11.6	38
112	39	44	38	-136.1	-138.5	-138.9	-137.8	1.5	20.3	31.8	16.4	20.8	8.0	6
113	56	49	47	-155.3	-148.9	-155.7	-153.3	3.8	19.6	42.9	15.3	21.7	14.9	7
115	40	47	39	-149.4	-150.6	-146.0	-148.7	2.4	24.9	22.0	20.2	23.1	2.4	9
116	39	28	24	-151.3	-154.7	-158.1	-154.7	3.4		13.0	18.2	16.5	3.7	<5
117	45	44	40	-137.9	-144.5	-141.5	-141.3	3.3	28.8	31.9	26.9	28.7	2.5	15
118	32	42	43	-149.5	-150.8	-145.2	-148.5	2.9	25.5	29.1	30.2	27.4	2.5	14
121	41	49	47	-148.5	-148.7	-154.3	-150.5	3.3	16.3	31.7	29.0	22.1	8.2	8
122	41			-135.4	-143.6		-139.5	5.8	19.9	35.9		23.1	11.3	<5
123	37	45	35	-144.7		-143.0	-143.8	1.2			38.4	38.4		24
124	44	47	41	-139.3	-134.6	-139.5	-137.8	2.8	17.4	21.1	19.8	18.6	1.8	<5
126	45	47	28	-143.1	-149.0	-142.8	-145.0	3.5	22.8	25.0	23.8	23.4	1.1	10
127	43	50	40	-144.3	-138.0		-141.1	4.5	23.0		17.4	21.2	4.0	7
128	48	49	45	-144.3	-146.7	-149.4	-146.8	2.6	27.6	31.2	18.5	25.5	6.5	12
129	45	45	45	-159.4		-161.2	-160.3	1.3	17.8		22.7	19.4	3.5	<5

**Table 5.** Atmospheric parameters (only available in electronic form)

Star	$T_{\text{eff}}(B-V)$ (K)	$T_{\text{eff}}(V-I)$ (K)	$T_{\text{eff}}(b-y)$ (K)	$T_{\text{eff}}(v-y)$ (K)	$T_{\text{eff}}(V-K)$ (K)	$T_{\text{eff}}(\text{phot})$ (K)	err (K)	$T_{\text{eff}}(H_{\delta})$ (K)	log $g$ (dex)	$v_t$ (km s <sup>-1</sup> )
1	8078	8102			7489	8090	12	7987	3.10	3.61
2	8140	8132			8372	8136	4	7904	3.05	4.50
4	9238	8604				8921	317	8801	3.23	3.18
5	9368	9496	9471	9502	9380	9468	31	9353	3.30	3.00
7	8325	8207			8244	8266	59	8335	3.18	3.40
8	8645	8864	9314	9111		9009	146	8883	3.24	3.22
10	8580	8642	8368	8553	8502	8539	59	8547	3.25	4.74
11	8350	8583	8683	8567		8550	70	8489	3.20	4.86
12	8061	8117			7977	8089	28	8072	3.15	3.40
13	8126	8220			8049	8173	47	8313	3.23	3.46
14	9110	9252	9049	9428	8534	9254	84	9404	3.36	3.12
15	8358	8809				8583	225	8547	3.21	3.00
16	8677	9272	8696	8676	8117	8799	147	8736	3.24	3.30
17	8475	8133	8300	8215	7677	8267	73		3.17	3.45
18	8252	8294			8249	8273	21	8389	3.24	3.39
20	8067	8179	8122	8075	7696	8104	26	8051	3.14	3.55
21	8066	8150	8123	8063	7354	8093	22	7978	3.11	3.63
23	8068	8178				8123	55	8190	3.17	3.46
24	8092	8429				8261	168	8244	3.16	3.45
25	8490	8867	8453	8532	8210	8575	95	8547	3.23	3.31
26	8071	8112	8170	8077		8101	23	8106	3.15	4.00
29	8475	8457			8089	8466	9		3.28	3.38
31	8302	8384			8326	8343	41	8369	3.25	3.35
33	9140	8386				8763	377	8712	3.31	3.20
34	8072	8153	8141	8048		8092	26	8218	3.18	3.46
35	8527	8580	8734	8556		8591	46		3.27	3.24
38	8995	8556			7932	8776	219	8729	3.32	3.30
39	8561	8707	8720	8565		8624	43	8610	3.23	3.73
40	8409	8498	8576	8407	8458	8459	41	8524	3.25	4.27
41	8378	8525	8655	8701	8209	8592	72	8616	3.29	3.34
42	8102	8173	8158	8130	7502	8139	16	8380	3.26	3.59
43	8183	8160	8192	8110	7766	8151	18		3.20	3.49
45	8447	8367			8097	8407	40	8462	3.25	3.35
46	8885	8734			8019	8810	76	8734	3.31	3.24
47	10128	9619	9306	9401	9302	9571	184	9416	3.34	3.50
48	8128	8396	8359	8408	8246	8340	66	8385	3.26	3.38
50	8313	8547	8412	8310	8023	8378	56	8494	3.25	3.40
51	8253	8444			8886	8349	95	8637	3.32	3.19
52	8751	8751	8757	8790	8691	8768	10		3.34	3.15
54	8083	8360	8222	8177	7549	8204	58	8386	3.24	3.58
55	8287	8634			7691	8461	173	8591	3.28	3.49
56	9364	8713			8765	9038	326	8707	3.30	3.04
60	8396	9098			7321	8747	351	8708	3.29	3.55
61	8587	8565			8862	8576	11	8620	3.34	3.19
62	10194	9499	9657	9602	9025	9711	156	9444	3.37	3.00
63	8463	8712	8345	8420	8376	8472	80	8417	3.25	3.28
67	9073	8809	8787	8628	10023	8785	92	8719	3.30	3.50
68	8460	8534			8938	8497	37		3.30	3.14
69	8297	8783	8522	8445	7632	8499	102		3.28	3.51
70	8348	8505			8319	8426	79	8510	3.30	3.28
72	8893	9295	9243	9196		9165	90	9036	3.35	4.14
73	8283	8140			7887	8211	72	8418	3.29	3.44
76	9738	8858			9178	9298	440	8768	3.30	4.50
77	8381	8531			8403	8456	75	8565	3.32	3.25
79	8756	8407			8636	8581	174	8634	3.31	3.64
80	8709	8947	8869	8836		8840	50	8770	3.31	3.15
81	8294	8314			8623	8304	10	8595	3.31	4.25
83	9266	9120			9377	9193	73		3.42	3.00
84	8351	8481	8605	8533		8501	54	8551	3.32	4.34
87	9276	8548			8873	8912	364		3.37	4.00
88	9344	9347				9345	2	9048	3.34	3.00
89	10369	9858			9195	10114	256	10169	3.52	3.00
90	8307	8531	8360	8365		8385	48		3.27	3.35
91	9244	9175	9179	8919	10332	9087	72	8820	3.31	3.00
92	8319	8164	8354	8332	8738	8300	43		3.28	4.22
94	9225	9596	9372	9401	9558	9399	76	9301	3.41	3.00
95	10044	9803	10315	9978		10024	106	9659	3.40	3.00
96	8960	9141	8827	9009	9309	8989	65	8925	3.36	3.00
98	8517	8413	8594	8484	9444	8498	37	8641	3.33	4.01
100	9572	10052			9444	9812	240	9670	3.42	3.00
102	8365	8284			8615	8324	41	8558	3.32	3.26
104	8485	8728	8776	8767	8643	8705	69	8683	3.34	3.21
105	9650	9797	9649	9537		9634	53	9737	3.48	3.00
106	8599	8733	8410	8593	8662	8586	66	8587	3.35	3.19
107	9141	9329	9444	9440		9359	71	9293	3.42	4.00
108	8751	8867	9066	8890	7550	8893	65	8802	3.34	3.41
110	8924	9246			8470	9085	161	9064	3.43	3.12
111	8444	8913			8246	8679	235	8676	3.39	3.32
112	9975	9572			9386	9774	202		3.51	3.00
113	10017	9391			9281	9704	313		3.55	3.00
115	10593	9637			9479	10115	478		3.56	3.00
116	11097	10215			9750	10656	441		3.60	3.00
117	9760	9048			8946	9404	356	9319	3.49	3.00
118	9292	9295	9459	9289	9674	9325	42	9338	3.50	3.00
121	9430	9784	9576	9872	9273	9707	100	9817	3.55	3.00
122	8957	9982				9469	513	9141	3.41	3.02
123	10393	9737	9818	9852		9930	150		3.53	3.00
124	9340	9613	9270	9217		9331	88	9591	3.53	3.00
126	9351	9651			9494	9501	150	9552	3.55	3.00
127	9890	9439	9731	9605	9744	9654	95	9750	3.57	3.00
128	9487	9791	9603	9762		9681	71	9729	3.56	2.50
129	10272	10180	10293	10160		10213	33	9968	3.53	4.50

**Table 6.** Abundances for individual stars (only available in electronic form)

Star	$Y_{NLTE}$	err	[Fe/H] <sub>I</sub>	[Fe/H] <sub>II</sub>	< [Fe/H] >	[N/Fe]	[O/Fe]	[Na/Fe]	[Mg/Fe] <sub>I</sub>	[Mg/Fe] <sub>II</sub>	[Si/Fe] <sub>II</sub>	[Ti/Fe] <sub>II</sub>	[Sr/Fe] <sub>II</sub>
Group A													
1			-1.73	-1.91	-1.82	0.74	0.71	0.13	0.73	0.36	0.58	0.44	-0.37
2			-1.66	-1.72	-1.69	0.53	0.42	-0.16	0.72	0.28	0.48	0.40	-0.20
11			-1.66	-1.77	-1.72	0.46	0.60	0.12		0.26	0.38	0.51	-0.23
12			-1.79	-1.83	-1.81		0.83	-0.01	0.74	0.52	0.80	0.43	-0.47
13			-1.67	-1.75	-1.71	0.74	0.71	-0.01	0.88	0.49	0.63	0.42	-0.55
15			-1.63	-1.91	-1.77		0.64	0.02	1.10	0.81	0.48	0.36	-0.44
17						0.32	0.49	-0.01		-0.06			
18			-1.95	-2.01	-1.98	0.74	0.61	0.01	0.51	0.28	0.53	0.41	-0.63
20			-1.74	-1.88	-1.81	0.53	0.53	0.01	0.29	0.76	0.50	0.34	-0.28
21			-1.78	-1.89	-1.84	0.69	0.60	-0.19	0.82	0.39	0.43	0.46	-0.49
24			-2.01	-2.07	-2.04		0.40	-0.07		0.77		0.16	-0.84
26			-1.61	-1.69	-1.65		0.36	-0.07	0.66	0.25	0.32	0.49	-0.11
31			-1.95	-2.11	-2.03		0.86	-0.05		0.14	0.22	0.20	-0.63
33			-1.95	-1.52	-1.73		0.71	-0.07		0.44	0.92		
34			-1.60	-1.82	-1.71	0.44	0.49	-0.09	0.83	0.35	0.55	0.33	-0.26
38			-1.75	-1.94	-1.85	0.64	0.72	-0.13		0.24	0.57	0.36	-0.45
39			-1.73	-1.96	-1.84		0.86	-0.05		0.08	0.61	0.49	-0.02
40			-1.70	-1.91	-1.80	0.65	0.71	-0.04	0.81	0.71	0.15	0.56	-0.46
41			-1.54	-1.60	-1.57	0.69	0.83	-0.06	0.86	0.93	0.58	0.49	-0.47
42			-1.90	-2.06	-1.98		0.58	-0.29		0.88	0.34	0.21	-0.63
43			-1.86	-1.81	-1.83		0.56	-0.12		0.27	0.41	0.48	-0.52
45			-1.83	-1.86	-1.85	0.52	0.69	-0.16			0.29	0.20	-0.43
48			-2.01	-2.02	-2.01	0.72	0.63	-0.23		0.74	0.65	0.23	-0.68
50			-1.68	-1.78	-1.73	0.71	0.61	0.02		0.39	0.54	0.30	-0.38
51			-1.82	-1.99	-1.91	0.64	0.75	0.03		0.03		0.35	-0.31
54			-1.94	-2.03	-1.98	0.52	0.67	0.04	0.59	0.14		-0.06	-0.32
55			-1.79	-1.99	-1.89	0.59	0.61	0.08		0.36	0.27	0.33	-0.59
56			-1.70	-1.47	-1.58			-0.06				0.53	-0.23
60			-1.87	-1.83	-1.85		0.67	0.02		0.52	0.28	0.32	-1.01
61			-2.06	-1.81	-1.94	0.54	0.72	-0.21		0.88	0.15	0.00	-0.73
63			-2.16	-1.85	-2.00	0.82	0.74	-0.09	0.55	0.52	0.20	0.14	-1.02
67			-1.85		-1.85		0.67	-0.02				0.19	-0.54
68			-2.08	-1.70	-1.89	0.89	0.65	-0.26		0.29	0.32	0.44	-0.90
69			-1.99	-2.14	-2.07	0.86	0.53	-0.16	0.87		0.52	0.35	-1.30
70			-1.96	-1.91	-1.94	0.76	0.75	-0.20	0.48	0.89	0.50	0.33	-0.63
73			-1.91	-1.75	-1.83		0.69	-0.22		0.09	0.51	0.34	-0.68
76			-1.91	-1.69	-1.80	0.66	0.68	-0.09		0.83	0.52		-0.43
77			-1.99	-1.89	-1.94	0.79	0.74	0.04	0.96		0.48	0.34	-0.75
79			-2.04		-2.04	0.63	0.81	-0.19		0.84	0.75	0.11	-0.66
80			-1.85	-1.93	-1.89		0.75	0.02		1.00		0.33	-0.28
81			-1.88	-1.69	-1.78		0.50	-0.05		0.78	0.40	0.29	-0.44
87							0.65	0.02		0.55			
90			-2.09	-2.18	-2.14	0.63	0.65	-0.15		0.65	0.99	0.29	-0.67
91			-1.91	-1.83	-1.87	0.93	0.53	-0.02		0.74	0.58	0.43	-0.56
92			-2.09		-2.09	0.67	0.69	-0.32		0.68	0.76	0.55	-1.08
98			-1.97	-1.76	-1.86	0.85	0.59	0.07		0.08	0.35	0.59	-0.50
102			-1.97	-2.09	-2.03	0.92	0.41	-0.29	0.72	0.29	0.35	0.34	-0.72
104			-1.92	-1.78	-1.85	0.87	0.68	-0.19		0.15	0.46	0.74	-0.53
106			-2.31	-2.01	-2.16		0.71	0.01		0.71	0.48		
Group B													
4			-1.60	-1.67	-1.63		0.78	0.31		0.70		0.66	-0.23
7			-1.69	-1.76	-1.73	0.98	0.46	0.30	0.66	-0.06	0.90	0.54	-0.43
8			-1.44	-1.66	-1.55	1.14	0.35	0.37		0.71	0.57	0.64	0.08
10			-2.06	-1.72	-1.89	1.19	0.84	-0.14		0.76	0.43	0.08	-0.28
14	0.27	0.08	-2.38	-1.69	-2.03	1.40	0.39	0.49		0.73	0.86		
16			-1.91	-1.96	-1.93	1.23	0.47	0.29			0.60	0.43	-0.41
23			-1.66	-2.04	-1.85	0.98	0.58	0.22	0.88	0.18	0.49	0.36	-0.35
25			-1.91	-1.86	-1.88	1.07	0.48	-0.01		0.52	0.29	0.44	-0.58
29			-1.96	-1.80	-1.88	1.13	0.73	0.03		0.49	0.66	0.31	-0.82
35			-1.95	-2.05	-2.00	1.19	0.54	0.25	0.73	0.14	0.38	0.29	-0.63
46			-1.73	-1.75	-1.74	1.01	0.64	0.23		0.53	0.76	0.43	-0.70
52			-1.79	-1.70	-1.74		0.82	0.15		0.78	0.52	0.44	
72	0.26	0.10	-1.83		-1.83		0.46	0.02		0.67		0.67	-0.46
83	0.43	0.06	-1.96		-1.96	1.16	0.54	0.24		0.76	0.53		
84			-2.13	-1.79	-1.96		0.49	0.19		0.61	0.44	0.40	-0.95
88	0.44	0.06	-1.85	-1.86	-1.86	1.22	0.19	0.15		0.54	0.56	0.24	-0.41
96			-2.28	-1.60	-1.94	0.99	0.40	0.03			0.52		-0.49
108			-1.86	-1.65	-1.76	1.01	0.69	0.23		0.79	1.32	0.51	-0.26
107	0.28	0.08	-1.71		-1.71	1.08	0.41	0.42		0.56	0.61	0.57	
111			-2.05	-1.80	-1.92	1.16	0.68	-0.03		0.67		0.75	-0.87
117	0.39	0.07	-2.05	-1.65	-1.85	0.92	0.53	0.30		0.84	0.45	0.63	
118	0.41	0.07				1.23	0.59	0.30		0.31	0.73		
124	0.42	0.05	-1.45		-1.45	1.05	0.44	0.34		0.05	0.48		-0.67
Group C													
5	0.41	0.06	-1.76	-1.56	-1.66	1.09	0.24	0.31		0.60	0.20		-0.41
47	0.36	0.07	-1.66	-1.91	-1.78	1.01	0.45	0.38		0.54	0.27		-0.03
62	0.27	0.08	-1.59	-1.49	-1.54	0.91	0.47	0.34			0.00	0.45	-0.75
89	0.32	0.05	-1.25	-1.83	-1.54	1.06	0.37	0.64			0.42		
94	0.28	0.08	-1.64		-1.64	0.97	0.83	0.12		0.31	0.69	0.39	0.06
95	0.41	0.05	-1.52	-1.84	-1.68	1.11	0.57	0.47		0.60	0.31		0.21
100	0.23	0.06	-1.65	-1.86	-1.76	1.10	0.36	0.21		0.47	0.14		0.12
105	0.34	0.06	-1.32	-1.70	-1.51	1.07	0.70	0.56		0.10	0.32	0.60	
110	0.44	0.05	-2.11	-1.64	-1.87	0.95	0.78	0.17		0.11	0.51		-0.48
112	0.30	0.06	-1.27	-1.91	-1.59	1.12	0.99	0.52		0.88	0.63	0.44	
113	0.43	0.05	-1.72	-1.63	-1.68	1.09	0.20	0.45		-0.27	0.44	0.38	
115	0.21	0.05				1.19	0.47	0.61		0.27	0.37		
116	0.20	0.04	-1.23	-1.57	-1.40	1.17	0.28	0.63		-0.06	-0.15		
121	0.26	0.06		-1.56	-1.43	1.01	0.80	0.50		0.71	0.29		
122	0.29	0.09	-1.77		-1.77			0.20			0.39		
123	0.25	0.06	-1.70	-1.46	-1.58	1.08	0.57	0.18			0.13		
126	0.44	0.05	-1.76	-1.78	-1.77	1.08	0.86	0.20		0.23	0.29		
127	0.37	0.06	-1.65		-1.65	1.15	0.52	0.48		-0.02	0.40	0.70	
128	0.30	0.06	-1.64		-1.64	1.08	0.38	0.55		0.31	0.50	-0.08	
129	0.36	0.05	-1.33	-1.59	-1.46	0.99	0.33	0.51		0.55	0.20		

**Table 7.** Average He abundances from the 5876 Å line for selected clusters

Cluster	[Fe/H]	Rel. Age (1)	$\log T_{\text{eff}}(\text{HB})$ Min	$\log T_{\text{eff}}(\text{HB})$ Median	$\log T_{\text{eff}}(\text{HB})$ Max	Ref.	N <sub>stars</sub>	$\log T_{\text{eff}}$ Range	$\langle Y \rangle$	r.m.s.
NGC1851	-1.18	0.81	3.73	3.74	4.08	2	19	3.95÷4.06	$0.297 \pm 0.020$	0.088
NGC2808	-1.18	0.83	3.75	3.92	4.57	3	17	3.96÷4.06	$0.336 \pm 0.013$	0.052
M 5	-1.33	0.85	3.76	3.89	4.18	4	15	3.95÷4.02	$0.312 \pm 0.017$	0.064
M 4	-1.18	0.97	3.72	3.76	4.04	5	6	3.95÷3.98	$0.295 \pm 0.011$	0.028
M 22	-1.70	1.06	3.82	3.97	4.22	6	29	3.95÷4.03	$0.338 \pm 0.014$	0.074
NGC6752	-1.55	1.02	3.82	4.02	4.47	7	4	3.93÷3.94	$0.252 \pm 0.016$	0.031

1. From Gratton et al. (2010); 2. Gratton et al. (2012a); 3. Marino et al. (2013b); 4. Gratton et al. (2013); 5. Villanova et al. (2012); 6. This paper;  
7. Villanova et al. (2009)

